The
University
Of
Sheffield.

Probing the mobile surface layer of confined polymer thin films by single molecule diffusion of fluorescently tagged poly(ethylene glycol)

By:

Ryan Colin Derek Jackson

A thesis submitted for the degree of Master of Philosophy

The University of Sheffield

The Department of Physics and Astronomy

Submission date: July 2017

Abstract

Surface and free diffusion of rhodamine-B poly(ethylene glycol) (RPEG) on a bare silicon substrate and a poly(ethyl methacrylate) (PEMA) thin film is investigated across a temperature range including the T_g of the PEMA thin film.

The glass transition temperature of poly(ethyl methacrylate) (PEMA) and polystyrene (PS) thin films are measured by ellipsometry. The diffusion of RPEG, measured with fluorescence correlation spectroscopy (FCS), as a function of temperature, is enhanced at the glass transition temperature of a PEMA thin film. It produces two broad peaks at different maxima at different temperatures. The RPEG appears coupled to the PEMA thin film as it approaches the glass transition temperature and has enhanced mobility however the precise mechanism for this is unclear due to irregularities with the results. Pure rhodamine-B dye and RPEG have 3D diffusion coefficients that are of similar order. This suggests that the two peaks are a result of dissociated dye.

DOSY NMR was used to measure the 3D diffusion coefficient for RPEG as a comparison to the FCS. The FCS and DOSY NMR results were a similar magnitude and order larger than the literature, it is likely that the polymer has degraded. FITC-dextran 3D diffusion coefficients, measured using the FCS equipment, were an order of magnitude larger than those in the literature. The similar disparity between measured values indicate a systematic problem with the FCS apparatus. FITC-dextran has shown a decreasing 2D diffusion coefficient as a function of temperature on a silicon surface.

New FCS equipment found the rhodamine-B and RPEG had similar 3D diffusion coefficients indicating the RPEG had dissociated. The 3D diffusion coefficient for FITC-dextran was in good agreement with the literature suggesting the previous FCS equipment requires servicing. There is a peak in 2D diffusion coefficient of FITC-dextran about the glass transition temperature for a thin film.

Declaration

I formally declare that this thesis is a product of my own work and any other work, either practical or literary, has been cited in a list of references or explicitly. No part of this thesis has been submitted for a degree, diploma, or other qualification at any other university.

Ryan Colin Derek Jackson

Acknowledgements

My most important acknowledgements go to my supervisors Professor Mark Geoghegan and Dr Matt Mears. Professor Geoghegan has been invaluable with his knowledge of polymer physics and wisdom with regards to research techniques and practice, allowing me to develop as an early researcher both independently and with a guidance. Dr Mears' understanding of all things related to this project and research are immensely appreciated. Dr Mears has definitely helped keep me sane this past year and my ability to complete this thesis and produce the work I have done is greatly owed to him. I thank both of my supervisors for the many hours they have sacrificed to help me with all things practical, research-wise and always being there to offer help when needed.

An acknowledgement to Dr Sandra van Meurs from the Department of Chemistry for her help with DOSY NMR, from educating me on how it works to carrying out the experiments. I would also like to thank Dr Ana Morales-Garcia for showing me many of the practical skills I required for this project, allowing me to learn and understand a wide variety of techniques. I'm also grateful she sacrificed so much of her time to help me with FCS work in the beginning to make sure I understood the protocol.

I'm very grateful that Ben Freestone showed me the Hellmanex cleaning method that solved a great deal of my polymer thin film preparation issues and our discussions about my thin film preparation helped resolve any issues I had. Yet again, he was another person who was also happy to drop anything he was doing to answer any questions or he'd offer a simple hello and would ask how things were going when we'd see each other around the department.

A similar comment can be made for Eleanor Dougherty. Ellie was very helpful with spincoating, polymer thin film preparation and ellipsometry, refining my technique so I could produce better samples. I appreciate that she would always ask how I was whenever we'd see one another that helped with me not getting too overwhelmed with work.

I would also like to acknowledge the help from my friend, May, who has been pivotal in anchoring me to the ground during this postgraduate research. Her support and encouragement has spurred me on to do the best that I can and she would always offer a welcome break to not get too flustered because of work. I truly appreciate all she has done for me.

Finally, an acknowledgement of particular importance is my family, specifically my mam and dad, Gillian and Steven. There is no amount of words that I could string together to explain how much I appreciate what my parents have done for me. Without them I would not be in the position I am in today, to be the first of my family to attend university and to work for a Masters. My accomplishments are their accomplishments and without their love and care for me I would not have had the drive to work as hard as I have done. I truly owe everything to them and I hope that this work is a small repayment for all they have done.

Symbols and Abbreviations

a	Monomer length
A	Initial amplitude of an electromagnetic wave
AFM	Atomic force microscopy
AG	Adam-Gibbs
b	Diffusion path length
b	Size of a compression blob
$B_y(z,t)$	Magnetic field
B_{0y}	Amplitude of the magnetic field
CRR	Cooperatively-rearranging region
c	Speed of light in a vacuum
$C(\boldsymbol{r},t)$	Spatial and temporal molecule concentration
δC	Local concentration fluctuation
D	Diffusion coefficient
D_{SE}	Stokes-Einstein diffusion coefficient
D_{Rouse}	Rouse model diffusion coefficient
D_{Zimm}	Zimm model diffusion coefficient
DOSY	Diffusion ordered spectroscopy
$E_x(z,t)$	Electric field
E_{0i}	Amplitude at boundary of incident electric field
E_{0r}	Amplitude at boundary of reflected electric field
E_{0t}	Amplitude at boundary of transmitted electric field
E_{0x}	Amplitude of the electric field
E_1	Heat of adsorption
$\boldsymbol{E}_{\mathrm{i}}$	Electric field incident on interface between two media
$\boldsymbol{E}_{\mathrm{r}}$	Electric field reflected from interface between two media
$\boldsymbol{E}_{\mathrm{t}}$	Electric field transmitted through interface between two media
$\boldsymbol{E}_x$	Electric field vector component acting in the x-direction

$\boldsymbol{E}_y$	Electric field vector component acting in the y-direction
F_{ads}	Free energy of adsorption
F_{int}	Free energy of interaction
FCS	Fluorescence correlation spectroscopy
FITC	Fluorescein isothiocyanate
FPEG	Fluorescein isothiocyanate-poly(ethylene glycol)
f	Force exerted on a particle as it is diffusing
f	Fraction of adsorbed particles diffusing two-dimensionally
f	Fraction of molecules detected in FCS experiment adsorbed to the surface
g	Number of monomers within compression blob
$G(\tau)$	Autocorrelation function
$G_{\mathrm{2D}}(\tau)$	Autocorrelation function for 2D
$G_{\mathrm{3D}}(\tau)$	Autocorrelation function for 3D
$G_{\mathrm{triplet}}(\tau)$	Autocorrelation function for the triplet state
H	Hydrogen
I	Intensity of light
I_0	Intensity at $(0,0,0)$
$I(t)$	Intensity at time t
$I(\boldsymbol{r})$	Excitation energy distribution
δI	Fluctuation in intensity
J	Diameter of compression blob cylinder
k	Wavenumber
k_{a}	Adsorption coefficient
k_{B}	Boltzmann constant
k_{d}	Desorption coefficient
L_{F}	End-to-end distance of an unconfined real polymer chain in mean field theory
L_0	End-to-end distance of an unconfined ideal polymer chain in mean field theory
$L_{\|\|}$	Ideal chain tube length in mean field theory

LCD	Liquid crystal display
LCL	Locally correlated lattice
$n_{1,2,3\ldots}$	Refractive index of
n_i	Refractive index of the medium an electromagnetic wave is incident
n_t	Refractive index of the medium an electromagnetic wave is transmitted through
N	Degree of polymerisation
N	Number of beads in the Rouse model
N_{ads}	Number of adsorption sites both vacant and filled
NMR	Nuclear magnetic resonance
OLED	Organic light emitting diode
P_{t}	Fraction of diffusing molecules excited to the triplet state
P_{v}	Vapour pressure
PEG	Poly(ethylene glycol)
PEMA	Poly(ethyl methacrylate)
PMMA	Poly(methyl methacrylate)
PS	Polystyrene
q	Fluorescence quantum yield
r	Radius of a spherical particle in Stokes-Einstein model
r	End to end distance of a polymer
r_{ij}	Reflection coefficient at interface between medium i and j
$r_{\perp}$	Amplitude reflection coefficient perpendicular to plane of incidence
$r_{\|\|}$	Amplitude reflection coefficient parallel to plane of incidence
$\mathbf{r}(\mathrm{t})$	Final position vector
$\mathbf{r}(0)$	Initial position vector
R	Molar gas constant
R	Radius of spherical confocal volume
R_{H}	Hydrodynamic radius
R_{total}	The total reflection coefficient

RFOT	Random first order theory
RPEG	Rhodamine-B-poly(ethylene glycol)
SE	Stokes-Einstein
$S(\boldsymbol{r})$	Optical transfer function
t	Time
t_{total}	Total measurement time
t_{ij}	Transmission coefficient at interface between medium i and j
$t_{\perp}$	Amplitude transmission coefficient perpendicular to plane of incidence
$t_{\|\|}$	Amplitude transmission coefficient parallel to plane of incidence
T	Absolute temperature
T_{c}	Crystalline transition temperature
T_{g}	Glass transition temperature
TPD	N,N'-bis(3-methylphenyl)-N,N'-diphenylbenzidine
V	Volume
V_{eff}	Effective volume
V_{f}	Free volume
$V_{\mathrm{f:vib}}$	Vibrational free volume
$V_{\mathrm{f:exs}}$	Excess free volume
V_{oc}	Occupied volume
V_{vib}	Vibrational volume
$W(\boldsymbol{r})$	Spatial parameter of intensity fluctuation
z	Number of molecules involved in mixing
x	Distance travelling by diffusing particle
α	Fraction of occupied sites in Langmuir's surface adsorption
α	Thermal expansion coefficient
α_{g}	Thermal expansion coefficient for a glass
α_{l}	Thermal expansion coefficient for a liquid
β	Ratio of adsorption and desorption coefficients $= k_{\mathrm{a}}/k_{\mathrm{d}}$

Γ	Structual parameter
δ	Adsorption energy per monomer
Δ	Ellipsometric parameter
Δ	Film thickness
ϵ_{ij}	Interaction energy between molecules i and j
η	Viscosity
η_{Z}	Viscosity in the Zimm model
η_0	Photon count
θ_{i}	Angle of incidence
θ_{r}	Angle of reflectance
θ_{t}	Angle of transmission
κ	Photon detection efficiency
λ	Wavelength of light
ν	Solvent quality parameter
ξ	Frictional coefficient
ξ_{bead}	Frictional coefficient of a bead in the Rouse model
ξ_{R}	Total frictional coefficient in the Rouse model
ξ_{Z}	Frictional coefficient in the Zimm model
ρ	Ellipsometric ratio of reflection coefficients = $r_{||}/r_{\perp}$
σ	Molecular absorption coefficient
τ	Relaxation time
τ	Experimental observation time
τ_{D}	Diffusion time
τ_{t}	Triplet state lifetime/diffusion time of fluorescent molecule before entering triplet state
τ_{2D}	Diffusion time in 2D
τ_{2Dx}	Diffusion time in 2D along the x-axis
$\tau_{\mathrm{2D}y}$	Diffusion time in 2D along the y-axis

τ_{3D}	Diffusion time in 3D
ϕ	Average volume fraction of a chain section
ϕ	Electromagnetic wave phase shift
χ	Flory interaction parameter
Ψ	Ellipsometry parameter
ψ_{ads}	Adsorbed chain thickness
ω	Angular frequency
ω_{xy}	Beam decay waist in (x, y) plane
ω_z	Beam decay height along z axis

Contents

CHAPTER 1: Introduction

Polymers have had an intertwined existence with humanity and civilisation, from the synthetic polymers that have shaped our technological advances to the biopolymers that allow life to thrive. We owe much to this form of soft matter and our developing understanding has allowed us to produce more beneficial polymer-based systems. Polymers are available in a variety of ways, from bulk solutions to nanoscopic thin films. There is a wide range of uses for polymer thin films – pharmaceuticals including hydrogels for drug delivery [1, 2], microfluidic devices and the coating industry [3], e.g. antireflection coatings i.e. LCD/OLED screens, lasers and other photovoltaic devices [4].

Due to their macromolecular architecture, polymers do not, regularly or as easily, form a crystalline structure when undergoing a phase transition from liquid to solid, they instead form a state of matter referred to as a glass. In layman's terms, the definition of a glass is one that exhibits solid-like properties but lacks the atomic long-range order found in crystals.

Materials that can crystallise have a characteristic temperature at which the phase transition occurs. Polymers, too, have a temperature at which they vitrify, aptly named the glass transition temperature, T_{g}. It has been shown consistently, via experimental research and simulation, that the properties of polymers diverge from their bulk behaviour when under confinement. Such properties include their relaxation dynamics [5] and their glass transition temperature [6, 7]. In the case of thin films, we usually restrict the polymers to the nanometre-length scale, typically via 1D confinement. There is a good understanding of what happens at the glass transition, but a unified theory of the processes and molecular mechanisms leading up to the glass transition has not yet been established.

Several factors are known to influence the value of the glass transition temperature: molar mass [8], molecular architecture [9], interfacial effects including the substrate-polymer interaction [10, 11] and thickness [12]. An Investigation into T_{g} for polystyrene thin films, of varying thickness, revealed thinner films had lower glass transition temperatures than the bulk value [6], it was hypothesised that there may exist a surface layer with more liquid-like mobility. After mounting evidence of this layer, it was suggested by de Gennes that we should not think of the glass transition temperature as a single value for the whole film but, instead, we should consider a distribution of glass transition temperatures throughout the film [13]. Since that initial suggestion, there have been a flurry of further simulations and experimental research that have supported this idea [14-16].

There have also been a variety of techniques used to probe this mobile layer and to develop our comprehension of the mechanisms behind it. This is intrinsically linked with our evolving understanding of the glass transition and the aforementioned factors that influence it. By understanding the distribution of T_{g} throughout the polymer thin film and how the mobile surface layer affects the diffusion of particles on the surface, we can enhance our development of thin films and produce more advanced films in the engineering and biological fields. This can be done by specifically tailoring each of the thin film to our exact specifications.

1.1 Aims for this work

Firstly, in chapter 1, a brief overview of the basics of polymers including their structure and dynamics will be provided [17, 18] to establish a way of understanding theories.

In chapter 2, the theory of the glass transition and single molecule diffusion will be analysed. Beginning with an overview of polymer models and their differences, the theory behind segmental dynamics and relaxation timescales will be addressed. After stating how we define the glass transition, a literature review on the progress made on the mechanisms of the glass transition and the factors that influence it will be conducted. Furthermore, the idea of the distribution of the glass transition and the evidence for the mobile surface layer will be explored. This work will compare different theories, simulations and experimental work that both support and contradict what has been theorised and seen [19, 20]. The mechanisms incorporate the models for the glass transition and fundamental principles behind polymers. Finally, there will be a consideration of the models and influences for single molecule surface diffusion.

In chapter 3, the experimental techniques of ellipsometry, fluorescence correlation spectroscopy (FCS) and diffusion ordered spectroscopy nuclear magnetic resonance (DOSY NMR) will be discussed. From their mechanical workings to the underlying mathematics that governs how they operate shall be reviewed.

For chapter 4, our own investigative research into measuring the glass transition temperature of thin poly(ethyl methacrylate) and polystyrene films shall be detailed using ellipsometry. With the use of FCS, the surface mobile layer will be probed as we increase the temperature of a thin film and monitor how the 2D diffusion coefficient of fluorescently tagged poly(ethylene glycol) changes. DOSY NMR will provide further evidence of the condition that the fluorescently tagged PEG is in.

Chapter 5 will conclude on the conducted research and summarise the work presented in the previous chapters.

1.2 Polymers: An Introduction

The microstructure of a polymer can be discerned by its etymology, with “poly” meaning “many” and “mer” meaning part thus a polymer is made of many parts. We define these individual parts as ‘monomers’, these are the repeating units within a polymer that are connected via covalent bonds. The total number of monomers is called the degree of polymerisation, *N*, and so the molar mass of the polymer is the product of the degree of polymerisation and the molar mass of the constituent monomers. The molar mass is equal to the mass of one mole – when there are an Avogadro’s number of molecules (6.02×10^{23} molecules mol^{-1}. Therefore, molar mass has the units of g mol^{-1} or *Daltons* (Da).

The simplest form of a polymer is a homopolymer where all monomers (denoted as *A*) are identical and arranged in a linear chain as shown in figure 1.1

… — A — A — A — A — …

Figure 1.1: Homopolymer of *N* monomers of molecule A arranged in a linear chain configuration.

For a real world example, we can consider the polymerisation of the molecule in Figure 1.2, where the R can be any chemical species. In the simplest case, the R groups would be hydrogen atoms, H, in which case, the monomer on the left would be ethylene and the resulting polymer would be polyethylene. The standard naming convention is "poly" and then the monomer from which the polymer has been created.

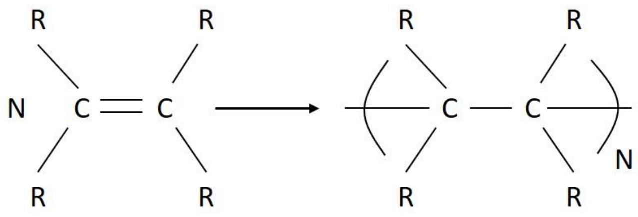

Figure 1.2 *N* ethylene molecules undergoing polymerisation to polyethylene with a degree of polymerisation *N.*

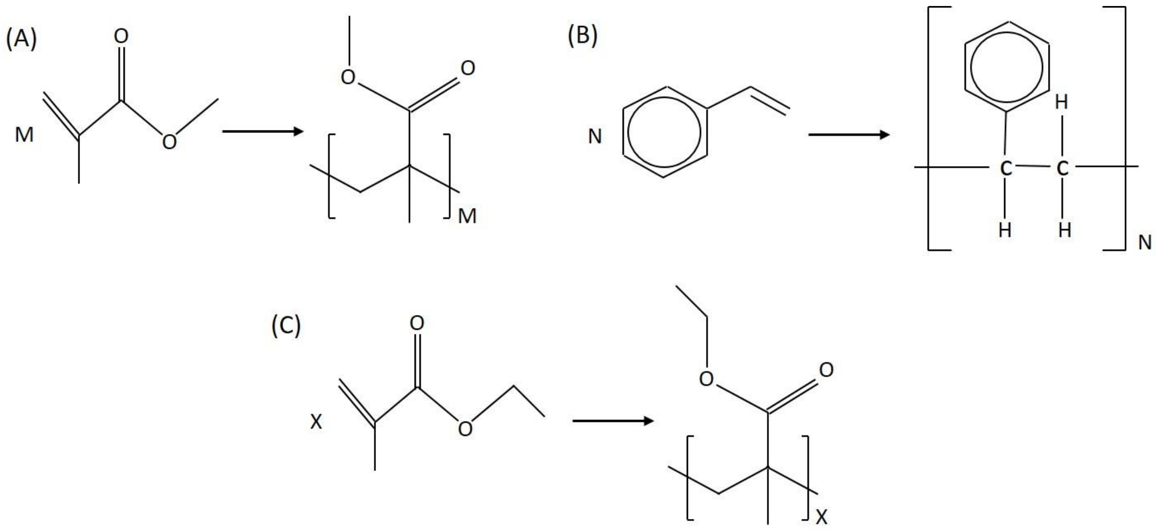

Figure 1.3: (A) *M* methyl methacrylate monomers undergoing polymerisation to form poly(methyl methacrylate) with degree of polymerisation *M*. (B) *N* styrene monomers undergoing polymerisation to form polystyrene with degree of polymerisation *N.* (C) *X* ethyl methacrylate monomers undergoing polymerisation to form poly(ethyl methacrylate) with degree of polymerisation *X*.

Other examples, of particular importance to this work, would be the monomers styrene and ethyl methacrylate which form polystyrene and poly(ethyl methacrylate) respectively (figure 1.3). Polystyrene needs no introduction, commonly associated with packaging in our daily lives, in 2015 there was close to two million tonnes of demand in Europe alone [21]. Poly(ethyl methacrylate) (PEMA) has a similar chemical structure to poly(methyl methacrylate) (PMMA) but with an extra methyl group and lower glass transition temperature. PMMA is often referred to as Perspex and has a demand of close to half a million tonnes in Europe in 2015 [21].

Polymer architecture also influences properties of polymer systems, such as a film. There are a variety of types of polymer architecture: linear chain (as mentioned previously), ring, ladder, randomly branched etc. A polymer network forms when there is a high degree of cross linking. Polymer conformations can then affect the properties after the polymerisation stage – this is defined as the "spatial structure of a polymer determined by the relative locations of its monomers" [17]. Other factors include, monomer interaction with each other and interaction with surroundings as we shall discuss in chapter 2.

For the last twenty years, a large amount of research has been dedicated to further our understanding on the glass transition. Although we have a well-defined understanding of what occurs upon reaching the glass transition, the mechanisms and processes leading up to vitrification are still debated. In this section, we shall review the microscopic detail of the glassy system, consider and compare the current models to describe the process of vitrification and we will discuss what factors influence the glass transition temperature – including what the theory predicts and what experiment evidence tells us.

CHAPTER 2: Theory

2.1 Diffusion

Unlike the glass transition, there have been some successful theories for diffusion. The process has benefited from over 100 years of developing theory, beginning with the studies by Brown in 1827 when observing the diffusion of pollen under a microscope [22]. One can apply a mechanical method of thinking to the dynamical system and form mathematical relationships from the observed behaviour.

By understanding the theory of single molecule diffusion, molecular mechanisms at play during the glass transition and the interactions with a surface can be inferred. Furthermore, the development of a theory of what operations occur within the surface layer can be ascertained. To understand the complexities of a single diffusing particle on a surface, one must develop a theory using the foundations of the simplest case and add layers of more intricate detail. The final goal is to have a thorough theory with the right assumptions such that we can model and predict the behaviours of any chemical molecule diffusing on a polymer surface. Beginning with the simplest case of 3D bulk diffusion (section 2.1.1), the assumptions of the diffusing molecule will be gradually removed to resemble polymer chains diffusing.

2.1.1 Stokes-Einstein (SE) Model

The simplest case is that of a solid particle, assumed to be a sphere, undergoing Brownian motion (see figure 2.2). This starting point assumes no interactions with other particles and surrounding medium. Following the standard derivation [18], first, consider a particle undergoing a random walk as shown in figure 2.1:

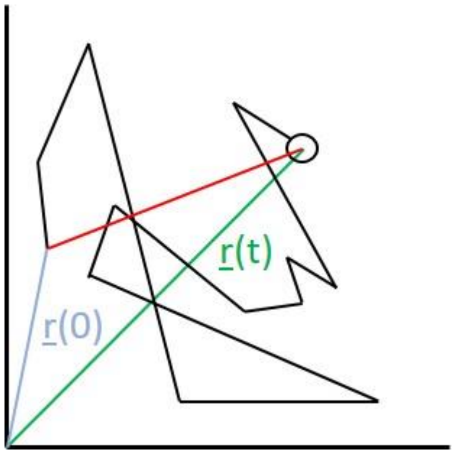

Figure 2.1: A random walk of a particle (sphere). Final position vector (green), $\underline{r}(t)$, and initial vector (blue), $\underline{r}(0)$, are defined from the origin of the coordinates to their respective positions. The end to end vector (red) is the difference between the final and initial vector.

In such a situation, the average of the displacement will always be zero due to the random nature of the system, however, the average of the square of the displacement will be proportional to the number of steps and therefore time. The mean-squared displacement of the particle, after time t, is given by:

$$\langle[\underline{r}(t)-\underline{r}(0)]^2\rangle = 6Dt\,, \tag{2.1}$$

where D is the diffusion coefficient of the particle undergoing random motion. As reported by Brown [22] the random motion of particles in a liquid must be a result of collisions executing a force on the diffusing particle. By considering the equation of motion for the system, that incorporates a drag force, the drag force will be proportional to the velocity of the diffusing particle, with a constant of proportionality, ξ. Physically, the interpretation of the constant of proportionality is that it is a representation of the interactions between the diffusing particle and its surrounding medium.

Using Stoke's law [23] for the viscous force on a spherical particle of radius r travelling through a liquid with viscosity η, assuming low Reynolds regime (small particles in viscous media), we find this frictional coefficient, ξ, as:

$$\xi = 6\pi\eta r\ . \tag{2.2}$$

Returning to the equation of motion for the diffusing particle. As the forces are random, each space dimension must be the same such that there is no acceleration. This is the approach that Einstein took when deriving an expression for the diffusion coefficient [24]. Assuming the particle is in local thermal equilibrium, the equipartition of energy theorem can be applied, thus he arrived at this relation:

$$D = \frac{k_{\mathrm{B}}T}{\xi}, \tag{2.3}$$

where D is the diffusion coefficient, k_{B} is the Boltzmann constant ($k_{\mathrm{B}} = 1.38064852 \times 10^{-23}\ \mathrm{m^2\ kg\ s^{-2}\ K^{-1}}$), T is absolute temperature and ξ is the frictional coefficient as defined in equation 2.2. Making a simple substitution of equation 2.2 into 2.3, we yield the Stoke-Einstein equation:

$$D_{\mathrm{SE}} = \frac{k_B T}{6\pi\eta r}\ \cdot \tag{2.4}$$

For molecular diffusion, the radius of the 'particle', r, is replaced with the hydrodynamic radius R_{H} – based on the average end to end distance. One can measure diffusion coefficients by dynamic light scattering and using equation 2.4 the size of the unknown particles can be deduced.

Varma and co-workers [25] derived an equation for the time taken, τ_{D}, to diffuse through a distance x with diffusion coefficient, D, as defined in equation 2.3:

$$\tau_{\mathrm{D}} = \frac{x^2}{4D}. \tag{2.5}$$

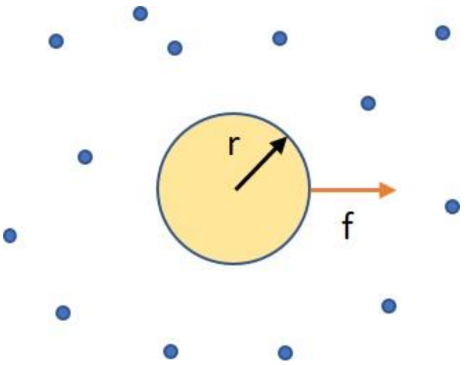

Figure 2.2 The Stokes-Einstein model of diffusion, central circle is spherical particle, of radius r, diffusing under a force f that is equal to the drag force. The smaller blue surrounding circles are the surrounding media (solvent) particles.

.

It is important to note that there are limitations to the SE formula due to its very simple approximations. There are suggestions that the SE relation should depend on viscosity, η^P ($P = 0.686 \pm 0.011$), as well [27]. This assumption is based on the diffusion of Xe atoms through liquid hydrocarbons at 20°C. It is better to think of the SE theorem as a starting point to build on for more realistic systems as discussed by work authored by Zwanzig *et al.* who also expand on the viscosity dependence and relate this to an effective hydrodynamic radius [26].

Simulations suggest that when the particle size of nanoparticles, suspended in polymer melts, is larger than the gyration radius of the polymer chain, the SE formula predicts the particle diffusion well [28]. This, however, breaks down when the diffusing particle is smaller than the polymer chain, since the diffusion depends on nanoviscosity rather than macroviscosity as is the case in the Stoke-Einstein formula. This supports the idea of a viscosity dependence but with specific attention paid to which viscosity we are referring to. A fractional Stokes-Einstein relation, where separate contributions from both the diffusing particle and surrounding media are considered, is another suggested modification of the Stokes-Einstein theory [29].

Temperature plays a key role also; the SE relation breaks down weakly in the high temperature regime and strongly at low temperatures [30]. This is a necessary consideration as we approach the glass transition and cooperativity increases, relaxation times increase and dynamic heterogeneity plays a larger role. The importance of these studies is that the SE relation is merely a first step to which we enhance and remove assumptions to apply a more complex system. There are limitations to what we can mathematically define due to the large number of molecules that exist in a system but we still endeavour to find a simplification in our models.

2.1.2 Rouse model

In the case of a linear polymer, we have to consider a series of small particles (representing the monomers). We can visually represent a polymer as a series of N beads coupled via springs as depicted in figure 2.3. The spring permeates interactions with other beads and each bead has its own frictional coefficient, ξ_{bead}, that it attains via the movement through the surrounding medium. There will be $N-1$ springs that can be mathematically represented as harmonic bonds. This model was first developed by Rouse [31].

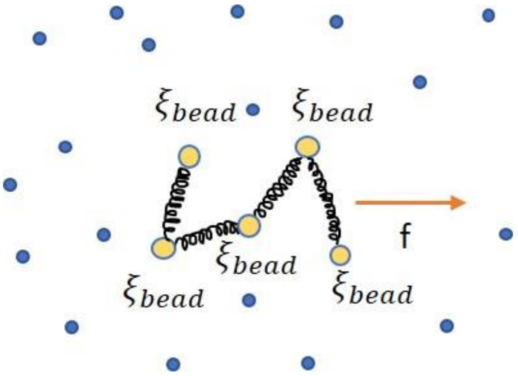

Figure 2.3 Visual representation of the Rouse model for polymers. The blue circles are the surrounding medium, the yellow circles with blue outline are the monomers of the polymer each with their individual friction coefficient connected via springs.

The main difference between the Rouse and SE models is now there are N independent spherical Brownian particles in the Rouse model. Two forces are exerted, the random force that is a result of the collisions and the frictional force. Both forces are exerted locally on each bead by the surrounding medium. Breaking the system down with an equation of state for each monomer, incorporating a frictional coefficient, the system is very similar to the SE model. The main difference for the Rouse system is that there are N friction coefficients. Assuming that all the beads are identical and they experience the same drag force, the total frictional coefficient ξ_{R} is

$$\xi_{\mathrm{R}} = \sum_{n_{\mathrm{i}}=1}^{n_{\mathrm{i}}=N} n_{\mathrm{i}}\xi_{\mathrm{i}} = N\xi_{\mathrm{bead.}} \tag{2.6}$$

Substituting this equation into equation 2.3 we find the diffusion coefficient for a Rouse chain, D_{Rouse}, to be

$$D_{\mathrm{Rouse}} = \frac{k_{\mathrm{B}}T}{\xi_{\mathrm{R}}} = \frac{k_{\mathrm{B}}T}{N\xi_{\mathrm{bead}}}. \tag{2.7}$$

The Rouse theory holds for short chains in a concentrated regime. As with the Stokes-Einstein model, there are continuous evolutions of the Rouse model. In 1988, the inertia of the beads was incorporated into the model [32]. The idea of free volume was included in the theory to account for good solvent quality by using a Gaussian repulsion between bead-spring chain [33]. The latter work is found to be in good agreement to a threshold value. The polymer and solvent can be considered as two separate phases with the polymer modelled as a dumbbell [34].

An extension to the Rouse model was proposed incorporating the inability of polymers to cross over each other. This was done using slip springs that are local, pairwise, invariant interactions both rotationally and translationally between polymer beads [35]. This model was tested further with experimental research [36] that showed that it was in good agreement with the Rouse model. The detailed dynamics of the beads in a Rouse chain have been explored through varied examples of forces applied and studying how the dynamics of the middle bead change over time [37], this was directly extrapolated on the diffusion model. An extension on the springs that connect each bead has been explored, considering a non-linear connection [38-40].

As we develop our theories of diffusion, we find for large molecules that we can still treat the system as a larger unit made of individual identical components, such is the case with the Rouse model and polymers.

2.1.3 Zimm Model

Zimm proposed that the diffusing particle is impeded by a drag force and undergoes a hydrodynamic interaction with surrounding medium particles [41] (see figure 2.4). For a polymer chain, the interaction can be between the individual monomers or with the solvent and monomer which induces a force on the solvent molecules. Within a certain volume the monomers will cooperatively move with the moving chain. The polymer is still modelled as a series of N beads connected via Hookean springs.

Consider the polymer chain and the interacting solvent as a solid sphere of radius r. The surrounding solvent particles not experiencing an interaction are unperturbed and are not considered. The end to end distance must depend on the degree of polymerisation and the monomer length, a

$$r \approx aN^{\upsilon} \ .$$

The degree of polymerisation is raised to a power, υ, that indicates solvent quality (equal to 0.6 for a linear chain in a good solvent). We use Stoke's law, again, to define the frictional coefficient, ξ_Z, of a chain, as described by the Zimm model, as it translates through a solvent of viscosity ξ_S:

$$\xi_{\mathrm{Z}} \approx \eta_{\mathrm{S}} r .$$

Following the same methodology as previously discussed, via substitution of this equation into the equation 2.3:

$$D_{\mathrm{Zimm}} = \frac{k_{\mathrm{B}}T}{\xi} = \frac{k_{\mathrm{B}}T}{\eta_{\mathrm{S}} a N^{\upsilon}} \ . \tag{2.8}$$

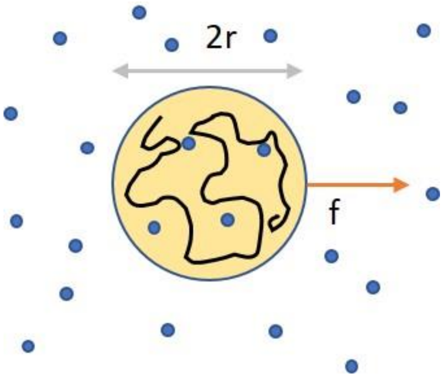

Figure 2.4: Visual representation of the Zimm model for diffusing particles. Here, the blue circles are the solvent particles, the thick black line is the polymer chain and the yellow circle is the sphere of hydrodynamic interaction.

The theme throughout this theoretical background is the emphasis on building on models from the most simplistic to real life representations. Of course, the main issue with real systems is the shear amount of factors that must be taken into account to the point where even the most powerful supercomputer won't be able to deal with it. Nevertheless, some advances have been made on the Zimm model.

A mean field theory of the Zimm model was developed specifically for single molecule experiments [42]. In addition, the model is extended for nonequilibrium monomer distributions. Fluorescently tagged single DNA molecules with polystyrene beads at the end of them were used. By directly, visually monitoring the relaxation of the molecule the model was reviewed and developed their mean field theory extension. It was found that the Zimm model holds for short to long range polymers far from equilibrium however it breaks down for longer chains becoming inhomogeneous.

An extension to this model for polymers confined by a harmonic potential has been produced [43]. Polymer chains when collapsed to their equilibrium conformation were investigated. The Zimm and Rouse model predicts the correct conformational behaviours in the cases where there is and is not a hydrodynamic interaction, respectively. Therefore, we can infer that this interaction only affects dynamics and not the equilibrium properties.

For longer chains (~100 monomers), individual polymer chains are unable to relax within the entire space therefore entanglement will occur due to crowding. To combat this problem, it was suggested each chain be surrounded by a tube which it is confined. The radius of the tube is then fixed by the density of entanglements among chains [44].

In the concentrated regime, it is suggested the chains can escape via a snake-like movement, that is called reptation [45]. For infinite chains, the reptation time scales with N^3. Experimentally, one finds $N^{3.4}$ due to fluctuations in the length of the tube [46]. One can accurately measure the diameter of this 'tube' by defining it as the mean square displacement over which the chains can react without encountering an obstacle [20]. It is important to note that in this regime, hydrodynamic interactions are unlikely to be relevant.

What is clear from the SE, Rouse and Zimm models is that they can predict the behaviour for very specific scenarios, such as those with short chains. For the purpose of this research, equation 2.5 will be used.

2.2 Surface Adsorption

An understanding of diffusion provides an initial insight into what properties are at play during two-dimensional surface diffusion. However, this alone has not tackled the effects of polymer chain surface adsorption in its full detail. Adsorption is one of the main influences during diffusion, depending on how strong the adsorption energy is will result in how a polymer will change its conformation and how able it is to diffuse along a surface. Therefore, an understanding of adsorption and how it arises, what parameters affect it and the effects on the polymer chains will aid with completing the picture of the underlying physical principles at work. Following a similar methodology used thus far, the simplest model will be established and then corrections are made by gradually removing assumptions until a model that applies to polymer chains is established.

The first step is to state how a surface is defined. The simplest form of a solid is a simple cubic lattice. It is assumed that the lattice extends infinitely in all directions and is free from defects. An infinite crystal has six neighbouring atoms. In the case of a surface, the surface is assumed to be completely smooth, no additional or missing atoms. The simple cubic lattice is now confined to two dimensions, with the surface of this lattice having five near neighbours of which four are on the surface. There is now an unoccupied bond on each of the surface atoms that would otherwise be occupied as before. These spare bonds allow for future interactions and offer the possibility of bond sites for adsorption.

Work published by Langmuir [87] was the first to characterise this adsorption based on spare bonds. The theory uses adsorption of vapour molecules onto a surface as the idealised model. The non-ideal case was then addressed in later work [88]. It is this that the building blocks of more developed models with added complexity can be established.

2.2.1 Langmuir adsorption

Langmuir’s treatment of adsorption (see figure 2.5) has several assumptions: adsorbed atoms do not interact with each other; each adsorption site is identical in terms of its physics and chemistry; the adsorbing atoms will only form a one atom thick layer and the mechanism each atom adsorbs to the surface is the same for all atoms. Additional assumptions that don’t directly relate to the spare bonds are that the adsorbate acts as an ideal gas and they have a strong affinity for the adsorption site only. The rate of adsorption i.e. the rate of increase in the fraction of occupied sites, α, is expressed as

$$\frac{d\alpha}{dt} = k_{\mathrm{a}} P_{\mathrm{v}} N_{\mathrm{adsorption}} (1 - \alpha) \tag{2.9}$$

where k_a is the adsorption coefficient, P_v is the vapour pressure and $N_\mathrm{adsorption}$ is the total number of adsorption sites both vacant and filled. The rate of desorption is independent of vapour pressure and is expressed as

$$\frac{d\alpha}{dt} = -k_\mathrm{d} N_\mathrm{adsorption} \alpha \exp\left[-\frac{E_1}{RT}\right] \tag{2.10}$$

where k_d is the desorption coefficient, E_1 is the heat of adsorption of the monolayer, R is the molar gas constant and T is the absolute temperature.

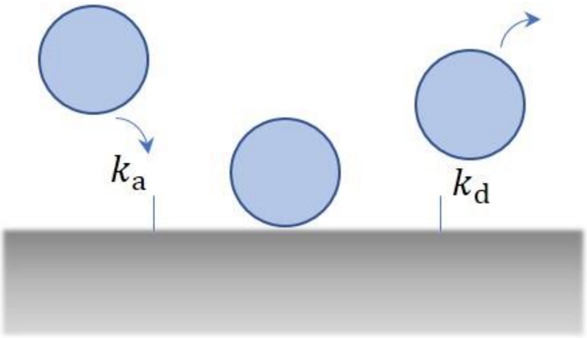

Figure 2.5: Depiction of Langmuir adsorption. The grey rectangle is the ideal surface, completely smooth and infinite in two dimensions. The blue lines represent the spare bonds on the surface where the middle blue line is missing as an atom has bonded to the surface and the spare bond now is occupied. The blue circles represent atoms assumed to be spherical in this illustration. The left atom is currently in the process of being adsorbed with adsorption coefficient k_a, the middle atom has been fully adsorbed and the right atom is undergoing desorption with desorption coefficient k_d. As shown only one layer of atoms are adsorbed.

The fraction of occupied sites can be found under the assumption that the system is in equilibrium. The two rate equations (equations 2.9-2.10) equated and rearranged yield

$$\alpha = \frac{\beta P_\mathrm{v}}{1 + \beta P_\mathrm{v}} \, , \tag{2.11}$$

where

$$\beta = \frac{k_a}{k_d} \, . \tag{2.12}$$

The ratio of the two coefficients, β, affects the equilibrium surface coverage. These coefficients, in turn, depend on the surface, gas and temperature of the system considered. Higher temperatures result in more energy to overcome the adhesive energy, gas atoms with a stronger affinity for the surface will have a larger β value and surfaces with large thermal energy will cause adsorbing atoms to desorb faster. These dependencies of β translate into any system, not just this idealised treatment. This theory does offer a useful starting point to build on with a very simple but effective visualisation of adsorption.

Where Langmuir's theory requires the first extension is correcting for the assumption that the adsorbates form a monolayer of atoms. Real systems, such as those involving polymer chains, require a theory that accounts for this. Brauner, Emmet and Tell (B.E.T.) published work that accounts for layers with more than one atom of thickness but treats each individual layer as though it would obey the same theory as Langmuir’s [88].

2.2.2 Polymer chain adsorption

Thus far, the interactions between atoms have been neglected but with long polymer chains, there are bountiful opportunity for interactions between monomers within chains and adjacent chains, although the latter is not as important for the single molecule system. Thence, in order to have a more robust and applicable theoretical model for adsorption of polymer chains, a revision must be made to address this. Changes that can refine the model include appreciating the interactions between atoms (both within a polymer chain and between polymer chains), entropy, polymer conformations and reviewing other parameters that affect polymer adsorption, all of which will be addressed in the following discussion.

Entropy at adsorption

Entropic considerations provide further issues to the Langmuir and B.E.T. models. When a chain adsorbs onto a surface it is localised and ‘locked’ into place. Reductions in entropy occur since there is a restriction in available polymer conformations and orthogonal to the surface the motion is restricted, hence conformational and translational entropy are reduced, respectively.

The spare surface bonds will attract polymer molecules within the vicinity of the surface. Surrounding atoms, when they get closer to the binding site, will begin to exert forces on one another. Atoms from other adsorbates and the surface atoms will also experience this force and possibly will be displaced from the surface. The entropy change from the displacement of other atoms could have a larger net effect than the reduction from the bound atoms.

Variables that affect polymer adsorption

A smooth surface, no interactions between atoms and no consideration for the specific adsorbate are recurring themes thus far. Moreover, the surface-adsorbate affinity strength and adsorbate conformation’s effect on the system are further omissions. In real systems, the aforementioned factors have a significant effect on the fraction of adsorption sites filled or left vacant. As each assumption is addressed and accounted for, a model that is applicable to real systems can be constructed that can produce the necessary predictions for systems that incorporate polymer adsorption.

The first assumption to require focus is the solvent in which the adsorbing molecules are immersed. There is an effect on the interfacial energy that will influence the amount of adsorption. There is an interaction parameter, χ, to quantify the interaction energies between identical and different molecules when each species exchanges a molecule [102]

$$\chi = \frac{z(2\epsilon_{\mathrm{AB}} - \epsilon_{\mathrm{AA}} - \epsilon_{\mathrm{BB}})}{k_{\mathrm{B}}T} \tag{2.13}$$

where z represents the number of molecules in the exchange process, ϵ_{ij} is the interaction energy between each molecule where in this example the two different molecules are labelled A and B.

In the total free energy of mixing, the entropy of mixing must also be accounted for and here it is assumed that the entropy of mixing does not overpower the energetic contributions as it has been reported [103]. The value of the interaction parameter gives insight into the favourability of mixing between two different molecular species. For $\chi > 0$, exchanging molecule A into the region of B molecules or vice-versa is energetically unfavourable as the free energy of the system will increase, demixing will occur. However, for $\chi < 0$, the opposite is in effect, the interfacial energy between similar molecules is now greater than the interfacial energy for dissimilar molecules, mixing is preferred.

Polymer chains adsorbing to a surface will reduce the amount of available polymer-solvent interaction points. A good solvent, for a given molecule, is defined by a preference of mixing between that molecule and solvent molecules. Adsorption allows for a reduction in polymer-solvent interaction in theta and poor solvents.

Secondly, real surfaces are never flat, completely smooth nor free from defects. The properties of the surface influence the affinity of atoms or molecules to the adsorption sites. If an adsorption site is more polar, polymers with a polar side group are more likely to adsorb to that surface [104]. Surface roughness is another factor, not only does this influence the surface area thus changing the number of adsorption sites but it also affects the interactions between the adsorbing polymer chains as depicted in figure 2.6.

A final parameter affecting polymer adsorption is the polymer size and conformation when adsorbed to a surface. To understand the effects of polymer size, a definition of 'size' is required. Polymers, even linear chains, are able to wrap round themselves, have different shapes and conformations which makes defining a size more difficult. There are two distinct categories, an ideal chain where monomers only interact with neighbouring sites and there is a real chain where all monomer-monomer interactions are accounted for. The latter has a special case, the θ-temperature, where a real chain can be treated as an ideal chain due to the monomer attractive and repulsive interactions cancel. The effects of polymer conformations are plentiful and thus require more detailed attention in the following sections.

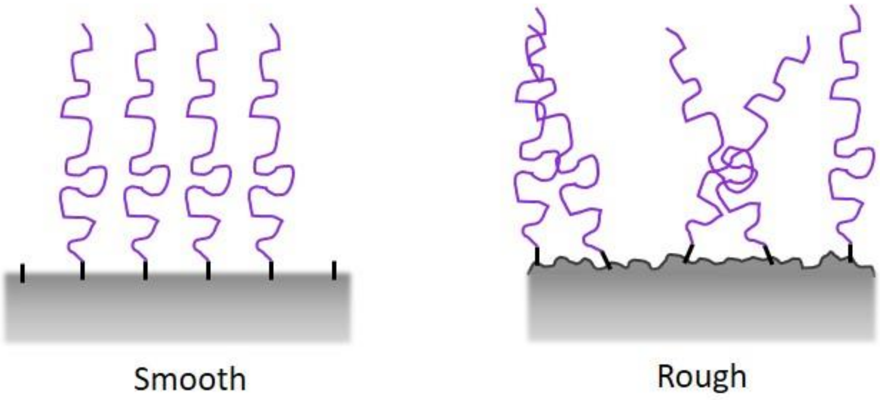

Figure 2.6: Illustration of how smooth and rough surfaces vary with adsorbing polymer chains. The surface is the grey, the thick, black lines are the bonds that an adsorbate can bind with and the purple lines are representing simplistic generic polymer chains. (left) The surface is smooth and free from defects. Each polymer chain is able to adsorb without influencing other chains too strongly. (right) A rough surface, with peaks and troughs that creates more surface area and more potential bond sites. Therefore, the polymer chains can overlap potentially and exert a greater influence with neighbouring chains.

de Gennes scaling theory

There are two different general mechanisms to describe the adsorption of polymers. The first is by de Gennes [125], which was originally for three-dimensional systems but can be adjusted for surfaces. The limitations for this theory are that it is only applicable for large molar mass chains in low concentrations, quite useful for single molecule diffusion.

For an adsorbed chain with thickness ψ_{ads}, there will be a characteristic length when a small section of the polymer chain has a total energy of interaction of order $k_{\mathrm{B}}T$. This characteristic length is referred to as an ‘adsorption blob’. The larger the adsorption blob, the larger the interaction energy, which in turn forces other chains onto the surface. Smaller lengths have a lower interaction energy and when this energy is less than the thermal energy of the system, it will be incapable of adsorption.

It is possible to determine an approximate size of the adsorbed polymer. Beginning with an assumption that the characteristic size, referred to as the ‘compression blob size’, is the length scale when the statistics of the chain sections compress into a cylinder of diameter, J, from an undeformed chain (see figure 2.7). This diameter can be written explicitly for the ideal and real chain (in a good solvent) systems

$$J \approx bg^{\frac{1}{2}} \qquad \text{(ideal chain)} \qquad (2.14)$$

and

$$J \approx bg^{\frac{3}{5}} \qquad \text{(real chain),} \qquad (2.15)$$

where b is the size of the compression blob and g is the number of monomers within the compression blob. The adsorbed chain has a conformation comprising a series of characteristic length sections that each approximate a compression blob. Therefore, the average volume fraction of a chain section, ϕ, is expressed as

$$\phi \approx \frac{b^3 g_{\mathrm{ads}}}{\psi_{\mathrm{ads}}^3} = \frac{b}{\psi_{\mathrm{ads}}} \qquad \text{(ideal chain)} \tag{2.16}$$

and

$$\phi \approx \frac{b^3 g_{\mathrm{ads}}}{\psi_{\mathrm{ads}}^3} \approx \left(\frac{b}{\psi_{\mathrm{ads}}}\right)^{\frac{4}{3}} \qquad \text{(real chain).} \tag{2.17}$$

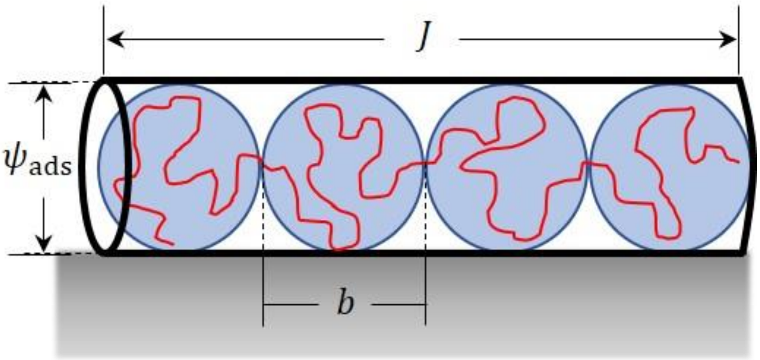

Figure 2.7: An illustration of the de Gennes scaling theory. The black cylinder represents the cylinder of diameter, J. The red line indicates a polymer chain adsorbed to the surface. The blue circles are the compression blobs of size b. The adsorbed chain has thickness ψ_{ads} from the surface which is illustrated as a grey rectangle.

Using the monomer number density, ϕ/b^3, and the volume of the layer within distance b, $\psi_{\mathrm{ads}}^2 b$, the total number of monomers within this characteristic length in contact with the surface can be approximated as

$$\frac{\phi}{b^3}\psi_{\mathrm{ads}}^2 b \approx \frac{\psi_{\mathrm{ads}}}{b} \qquad \text{(ideal chain)} \tag{2.18}$$

and

$$\frac{\phi}{b^3}\psi_{\mathrm{ads}}^2 b \approx \left(\frac{\psi_{\mathrm{ads}}}{b}\right)^{\frac{2}{3}} \qquad \text{(real chain).} \tag{2.19}$$

Next, the total energy gain per adsorption blob can be defined as

$$\delta k_{\mathrm{B}} T \frac{\psi_{\mathrm{ads}}}{b} \approx k_{\mathrm{B}} T \qquad \text{(ideal chain)} \tag{2.20}$$

and

$$\delta k_{\mathrm{B}}T\left(\frac{\psi_{\mathrm{ads}}}{b}\right)^{\frac{2}{3}} \approx k_{\mathrm{B}}T \qquad \text{(real chain),} \tag{2.21}$$

where δ is the adsorption energy per monomer. Each of equations 2.20 and 2.21 are of order $k_{\mathrm{B}}T$ due to the initial conditions for the characteristic lengths to exist. Via rearrangement of the equations, the adsorption blob (characteristic length of adsorbed chain) can be defined as

$$\psi_{\mathrm{ads}} \approx \frac{b}{\delta} \qquad \text{(ideal chain)} \tag{2.22}$$

and

$$\psi_{\mathrm{ads}} \approx \frac{b}{\delta^{3/2}} \qquad \text{(real chain).} \tag{2.23}$$

The free energy of adsorption of a chain can be approximated as

$$F_{\mathrm{ads}} \approx -k_{\mathrm{B}}T\frac{N}{g_{\mathrm{ads}}} \approx -k_{\mathrm{B}}T\delta^{1/(1-\nu)}, \tag{2.24}$$

this free energy depends on the fractal dimension of a polymer chain, ν, whose value depends on the chain in question, for ideal chains $\nu = 0.5$ and for real chains $\nu = 0.6$.

Mean-field theory

Another theoretical approach to how polymers adsorb to a surface is the mean-field theory. This model aims to allow for the measurement of values that can then be fitted to the approximations provided in this framework. As the theory name suggests, a mean field is required, hence concentrated solutions are necessary. The biggest drawback about this model is the assumption that the concentrated polymer regime is the largest factor in the properties of the adsorbed chain.

Firstly, the distance between the surface and monomers is uniformly distributed up to an adsorption thickness, again, defined as ψ_{ads}. It can therefore be stated that the fraction of monomers touching the surface within a distance b is b/ψ_{ads} and the total number of monomers contacting the surface is Nb/ψ_{ads}.

The free energy of interactions for the surface and all contact monomers will be

$$F_{\mathrm{int}} \approx -\delta k_{\mathrm{B}}TN\frac{b}{\psi_{\mathrm{ads}}}. \tag{2.25}$$

Although there is an energetic gain during this chain adsorption, there will be an entropic cost as the confinement reduces available conformations and movement. The length of occupied space by an ideal chain is the length of a tube $L_{||}$. This tube is independent of confinement because each monomer acts independently. The characteristic length will have a random walk equal to N/g and the tube length can be approximated to this. Substituting this random walk into equation 2.14 the length of the tube is

$$L_{||} \approx L\left(\frac{N}{g}\right)^{\frac{1}{2}} \approx bN^{\frac{1}{2}} \tag{2.26}$$

There will be repulsion between the chains in real systems and this must be addressed. The repulsion will effectively remove other surrounding chains from the tube hence no overlap will occur, this gives the tube length an order of N as follows

$$L_{||} \approx L\left(\frac{N}{g}\right) \approx \left(\frac{b}{L}\right)^{\frac{2}{3}} Nb \quad . \tag{2.27}$$

The confinement energy of an adsorbed chain is $\approx k_{\mathrm{B}}T$ per compression blob hence the total confinement energies for ideal and real chains are

$$F_{\mathrm{conf}} \approx k_{\mathrm{B}}T\frac{N}{g} \approx k_{\mathrm{B}}T\left(\frac{L_0}{L}\right)^2 \qquad \text{(ideal chain)} \tag{2.28}$$

and

$$F_{\mathrm{conf}} \approx k_{\mathrm{B}}T\frac{N}{g} \approx k_{\mathrm{B}}T\left(\frac{L_{\mathrm{F}}}{L}\right)^{\frac{5}{3}} \qquad \text{(real chain),} \tag{2.29}$$

where L_0 and L_{F} are the the end-to-end distances of ideal and real unconfined chains, respectively. Adding the free energy of confinement to the interaction energy (equation 2.25), the total free energy of an adsorbed chain can be written as

$$F_{\mathrm{ads}} \approx k_{\mathrm{B}}TN\left[\left(\frac{b}{\psi_{\mathrm{ads}}}\right)^2 - \frac{\delta b}{\psi_{\mathrm{ads}}}\right] \qquad \text{(ideal chain)} \tag{2.30}$$

and

$$F_{\mathrm{ads}} \approx k_{\mathrm{B}}TN\left[\left(\frac{b}{\psi_{\mathrm{ads}}}\right)^{\frac{5}{3}} - \frac{\delta b}{\psi_{\mathrm{ads}}}\right] \qquad \text{(real chain).} \tag{2.31}$$

An optimal adsorption thickness can be found from the minimum of the total adsorption free energy equations

$$\frac{\delta F_{\mathrm{ads}}}{\delta \psi_{\mathrm{ads}}} = 0$$

that yields

$$\psi_{\mathrm{ads}} \approx \frac{b}{\delta} \qquad \text{(ideal chain)} \tag{2.32}$$

and

$$\psi_{\mathrm{ads}} \approx \frac{b}{\delta^{3/2}} \qquad \text{(real chain).} \tag{2.33}$$

Referring back to equations 2.22 and 2.23, the above ideal thicknesses are identical in both theories. This yields an identical expression for the total adsorption energy,

$$F_{\mathrm{ads}} \approx k_{\mathrm{B}} T N \delta^{1/(1-\nu)} \quad . \tag{2.43}$$

2.3 The Glass Transition

2.3.1 The Basics of the glass transition

Solids and liquids are familiar concepts that are taught early on in education. Visually, we can represent these states of matter as an arrangement of spherical particles and their interlinking bonds as lines. An example of the arrangements for both a liquid and a crystalline solid can be seen in figure 2.8. For a liquid, the particles possess random orientation and lack long-range order, they are free to move around one another. For a solid, the particles are locked into a correlated structure but are free to vibrate about their equilibrium position and no translational movement can occur. Another way to think of the defining properties of solid and liquid are their volumetric tendencies. A liquid will assume the volume of a container within the limits of its own volume whereas a solid will remain stationary within its own dimensions.

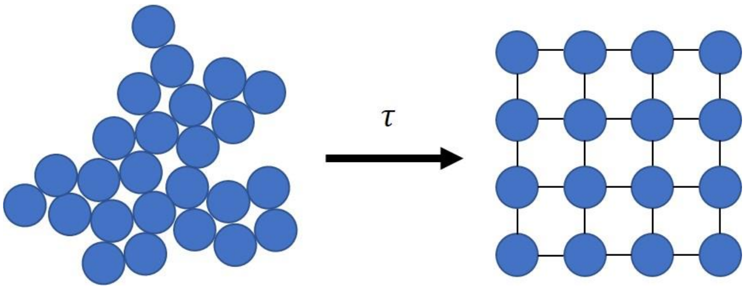

Figure 2.8: Crystallisation of a liquid (left) using spherical particle representation, to a crystalline solid (right). The process occurs in a characteristic relaxation time, τ.

Now we consider the phase transition from a liquid to a solid via crystallisation. Imagine we have the arrangement shown on the left-hand side of figure 2.8. As we reduce the temperature of the system, we remove kinetic energy from the liquid particles. They will move to acquire positions that result in the minimum free energy of the system – their equilibrium positions – the particles form stable interatomic bonds. At the transition temperature, the liquid phase is metastable, via nucleation and expansion of crystalline domains a phase transition occurs. There are interfacial energetic costs that arise from the domains forming. This is the resultant crystalline structure. The time it takes for the particles to relax, and find the orientation and configuration with the minimal free energy, is the relaxation time, τ, which varies depending on the material.

We can experimentally see this effect via measurements of volume as a function of temperature. Volume is a more measurable thermodynamic quantity and it is easier, conceptually, to explain what is causing the volume of a sample change in comparison to energy or entropy. As expected, when we reach the glass transition temperature, there will be a sharp decrease in volume. This is a discontinuity in the temperature volume profile. We can exploit this discontinuity in determining the transition temperatures (figure 2.9).

By increasing the cooling rate and removing the thermal energy quickly, the particles are not given adequate time to relax, they are out of equilibrium. There is not sufficient time to nucleate and grow a crystalline phase. The particles must condense to whatever conformation they possessed at the time – this is the glass transition. There is an induced molecular motion slowdown. There is no discontinuity but a continuous reduction in volume. As depicted in figure 2.9, the glass transition occurs at a distinct glass transition temperature, T_{g}, however in actuality there is a glass transition region. As we decrease the cooling rate, the glass transition temperature decreases.

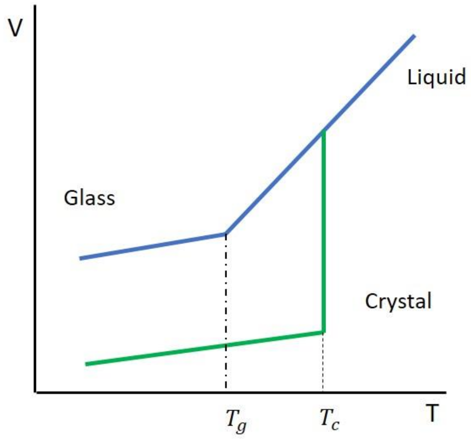

Figure 2.9: Volume (V) – Temperature (T) relationship for crystalline materials and glassy materials. There is a discontinuity at the phase transition temperature, T_{c}, for the crystalline (solid-liquid) phase transition. There is no gradual decrease in volume for the glass system, with a change in gradient upon glass transition at its characteristic glass transition temperature, T_{g}.

The glass transition is not a true thermodynamic phase transition because there are no discontinuous changes in a physical property [47]. The transition is purely kinetic. An important concept is the idea of relaxation time, this plays a vital role in the glass transition. We find that the segmental time which follows changes in molecular mobility increases rapidly upon cooling, as we would expect. Furthermore, there are two different definitions of glass transition temperature. There is the thermal T_{g} which is defined from a thermodynamic point of view and the dynamic T_{g} is defined from kinetics, such as the consideration of segmental dynamics.

2.3.2 Theories and models of the glass transition

There are a wide variety of theories that try to explain the dramatic reductions microscopic mobility that induce such a reduce in viscosity and increase in relaxation times. Energetically, we can think of the glass transition as when the energy landscape of the system becomes more jagged as temperature is decreased, developing canyons and wells of increasing depth [20, 48]. If the energy landscape were to be mapped to an (x, y) plot, the x-axis would be the position in the molecular system and energy would be plotted along the y-axis. This energy landscape can be thought of more easily if we think of the solid-crystalline version, in this the energy landscape would develop wells and valleys of a more structured order and defined positions and not as rugged. This energy landscape way of thinking is useful as the characteristic defining property of the glass transition is the interplay with energy considerations.

Firstly, the Adam-Gibbs (AG) theory [49] uses the energy landscape via cooperative dynamics. This entails cooperative rearrangement of particles in the system as they move through the energy landscape. There is a temperature dependence on size of the cooperatively-rearranging regions (CRRs). This is what determines the energy barrier to allow a phase transition. These CRRs describe the minimum number of molecules that must move cooperatively in order for motion to take place.

Secondly, the Random First Order Transition (RFOT) [50, 51] theory suggests that a system is more like a mosaic of disordered subsystems that are in contact with one another. Similar to the AG theory, the structural rearrangement free energy scales with the subsystem size raised to a power.

Thirdly, there is the Dyre shoving model [52], which treats the system more as a solid than a liquid and assumes that most of the molecular motion is vibrational. Once sufficient local work has been done on the particles by the particles vibrating, their displacement can occur enabled by an increase in free volume. The work done requires that nearby molecules shove against their surroundings. This rapid vibrational motion resembles the behaviour of an elastic solid.

A theory that is returned to frequently, due to its simplicity and scope for development, is the Free Volume Theory by Fox and Flory [53] that was later refined by Turnbull [54]. Although similar to the AG theory, it does not in fact contain any consideration of cooperativity. This theory suggests the kinetic mobility of the fluid depends on its free volume [20]. The free volume is the additional volume required to undergo translational and rotational motion by a molecule. Free volume is easily defined microscopically and so can be used to define how glassy a system is.

Returning to determining T_{g}, as we discussed before, we can measure volume as a function of temperature. When we measure the volume of the system we are measuring the contributions from the excluded volume occupied by the molecule, V_{oc}, and the remaining contribution is from free volume V_{f}:

$$V(T) = V_{\mathrm{oc}}(T) + V_{\mathrm{f}}(T)\ . \tag{2.7}$$

The temperature dependence from the excluded volume arises from the molecular vibrations increased amplitude and for rotational and translational motions required at higher temperatures where more motion is necessary. Vibrational nature does not depend on freedom of motion therefore has no phase dependence and thus displays no discontinuities at the phase transition. We expect a discontinuity in free volume.

By measuring the change in volume as a function of temperature, one cannot easily distinguish the different contributions of V_{oc} and V_{f}. Therefore, it is often easier to measure viscosity and infer changes of the free volume from that. Nevertheless, there is continued evidence that there is a close correlation between T_{g} and free volume for different glass-forming polymers [55]. A locally correlated lattice (LCL) model can be used to find the free volume in bulk far from T_{g} and then extrapolate to the glass transition temperature. It was with this method that the correlation between T_{g} and free volume is developed. The T_{g} values are experimentally measured since the LCL model itself does not predict the glass transition which is a drawback to this method. By taking the LCL equation of state and fitting it to experimental pressure-volume-temperature data, the free volume available in the system can be calculated. By comparison with measured glass transition temperature of 51 polymers, they found that there is a linear correlation with glass transition temperature and free volume. It was also suggested that temperature itself plays a major role in the glass transition.

Recently published data suggests there is a correlation between free volume and relaxation times (dynamics) of glasses [56]. For a fixed temperature, the logarithm of relaxation times is linearly proportional to the inverse of free volume. The linear relationship suggests a connection between liquid equilibrium thermodynamic properties and dynamic relaxation. This again uses the LCL equation of state. It is interesting to entertain the possibility that free volume availability dictates the relaxation dynamics of glass forming liquids. The limited free volume will result in longer relaxation times and thus form a glass more readily.

There is, in fact, a correlation between all the theories discussed this far. They display that a glassy system will exhibit ‘dynamic heterogeneity’. We can consider the system as being made up of smaller distinct sections which are governed by their own local dynamics as opposed to that in the bulk [57, 58]. However, it is experimentally difficult to observe this phenomenon for glassy systems. It has been possible to show via simulation that there exists a cluster-like pattern of ‘fast’ and ‘slow’ particles that exists within a system [59, 60]. This suggests that there are indeed differences in local dynamics that are segregated from one another. This is appealing as it resembles the idea of nucleation and growth of crystalline domains. When one considers how glasses as a snapshot of uncorrelated liquid order, the idea that there do exist pockets of different dynamics within the system is logical.

Building on the idea of dynamic heterogeneity, there are other models that consider how liquids assemble into preferred local structures as they cool. One such set are the frustration models, that link competing structural aspects to glassy behaviour, that has been reviewed in detail [61]. With this model, there is a locally-preferred molecular order that expands to a limit thus promoting finite length scale molecular cooperativity. This again reflects the idea of heterogeneity within glassy systems but provides a potential reasoning behind it. The frustration stems from the inability to continue growing and this molecular slowdown on the mesoscopic scale can help explain the tremendous increase in viscosity that we see with glassy systems.

2.3.3 Parameters that can infer T_{g}

The models described in the previous subsection are useful, but it is difficult to theoretically predict a glass transition temperature, for a given history and cooling rate, due to the energy landscape being extremely large and complex. It is therefore easier to measure a glass transition temperature with a selection of methods available. The basic concept is to look for a microscopic quantity to pass a predefined threshold value.

As volume is a more easily accessible and measurable thermodynamic property, it is customary to use volume as an indicator for identifying a phase transition. An equation of state approach has been developed [62] where the model can be fitted to a known property, such as volume of a sample, which leads to predictions for other properties inaccessible by experiment and to predicting the glass transition temperature of thin polymer films. The glass transition temperature of a specific material can be defined as when the sample-averaged volume drops below that of the bulk glass value. This model is specific to polymer films and takes into consideration the effect of surface layers and interfacial interactions. There are some drawbacks to this method, understandably. It does not consider the effect that moving from bulk to thin film has on the temperature dependence of volume. The results indicate no molar mass dependence. The study does not address substrate-supported polymer thin films, only freestanding films and hence development of this theory is needed.

For films, their thickness as a function of temperature can be plotted. The glass transition temperature is defined as the point where the gradient increases, signalling a phase change from the glassy state to the melt/liquid state [63, 64]. There are several methods for determining the exact glass transition temperature that will be discussed in detail in 4.2.

2.3.4 Factors affecting T_{g} and the mobile surface layer

Importantly, when developing models for the glass transition and the effects it has on the properties of polymers and their thin films, one must consider what affects the glass transition and what properties it changes. Of interest to researchers of polymer thin films is the effect of confinement and interfacial interactions e.g. polymer/substrate interactions and free surfaces. For the case of polymer films, we can confine them to the nanometre length-scale, often supported by a substrate e.g. silicon or glass. For many years, we have investigated this area and the effects it has on the polymer physics [65, 66].

Let us consider the effects on polymer properties when under confinement where interfacial effects play a large role. Here we are confining at least one dimension to be within 100s of nm in thickness. Not only is the position of the glass transition altered in this case from bulk values but also the dynamics of the system. This plays an important role for the applications of polymer films as understanding how the properties change can lead to greater definition and reliability. There is a greater deviation from the bulk due to the larger contribution from the interface.

Chain conformations are altered during the glass transition temperature [67, 68]. An example of this considers entropic and energetic contributions to the equilibrium concentration formed by compressible polymer melts near solid neutral, attractive and repulsive walls [68]. For low concentrations, it is found that the density profile grows linearly near the wall and becomes exponential approaching the bulk. This establishes the behaviour of polymers near surfaces and how their conformations will change depending on the strength of the attractive and repulsive forces present, a necessary consideration when forming polymer thin films.

Thin films have a high surface-to-volume ratio hence interfacial effects dominate their behaviour. We can review the substrate-polymer interactions via the work by Keddie et al. [10] who helped initiate this discussion. They considered the thickness dependence of the PMMA glass transition temperature. They then looked at two different substrates and the effect this had on the thickness dependence. They found with native oxide of a silicon substrate there was a slight increase in T_{g} with decreasing thickness and attributed this to hydrogen bonding at interface between the hydroxy groups on the silicon and the highly electronegative oxygen atoms in the methacrylate side chains permitting hydrogen bonding. One can say the PMMA is attracted to the substrate and this restricts the chain mobility, thus leading to an increase in T_{g}. The second substrate was silicon onto which gold was evaporated. Here it was found that T_{g} decreases with film thickness as was the case for PS on hydrogen-passivated silicon [6]. Using similar logic to before, the PMMA is not as attracted to this surface due to their being no hydroxy groups which the oxygen atoms in the methacrylate sidechain can bond to, hence there is no restriction on chain mobility and so T_{g} decreases. As for the PS work, this suggests there is liquid-like layer whose size diverges as T_{g} is approached from below, a direct consequence of enhanced chain mobility.

Another factor that affects the value of T_{g} is the cooling rate. By varying the cooling rate, one can control the deviation from bulk glass transition temperature (by ‘bulk’ we are referring to those polymers not under nanoscale confinement) [69]. Altering the cooling rate and using ellipsometry to measure the thickness dependence of the glass transition temperature, it was found that with the slowest cooling rate (1 K/min), there was a reduced T_{g} below the ‘bulk’ value. After increasing the cooling rate, the reduction in T_{g} reduces, once at 90 K/min, there was no apparent thickness dependence of T_{g}. There is also a broadening of the transition at lower cooling rates and a narrowing of transition at the higher cooling rates leading to a smaller T_{g} reduction. The thicknesses of the polystyrene films used, ranged from 5.5-90 nm.

It is important to note that the changes in glass transition temperature values are often with very small film thicknesses, as film thicknesses increase to hundreds of nanometres, the gradient of the glass transition temperature change lowers. However, it is important that we understand ultrathin films as they allow us to probe properties such as segmental dynamics which would otherwise be lost in bulk average motion.

Molecular dynamics simulations have explored the influence on structural relaxation, upon cooling, from the surface in a free-standing polymer film [70]. The model uses bead-spring chains in which each has *N* monomers. It considers when monomers can interact among the backbone and when they cannot. They find the monomers at the free surface exhibit faster relaxation than in the bulk at the same temperature. There is a characteristic length over which the relaxation difference continuously changes into that of the bulk. This simulation supports the idea of a liquid-like surface layer. By looking at nonentangled and slightly entangled chains it is found that both have film dynamics that are spatially heterogeneous i.e. monomers at free surfaces relax faster than in the bulk. The simulations also looks into the effects of weak polymer-substrate interaction. Substrates with a weak interaction have a reduced sample average glass transition temperature due to the monomers at the free surface and weakly interacting substrate having enhanced mobility causing faster dynamics.

A review on simulations analysing the glass transition by Baschnagel and colleagues [71, 72] explored the effects of surface roughness on the dynamics of polymer thin films. For smooth repulsive interfaces, it is found that there is no molecular structure hence the short ranged repulsive interactions. Molecular order is promoted orthogonal to the surface which induces a more concentrated layer of monomers. The excluded volume of the monomers within the layer creates a locality immediately alongside this layer which is absent of monomers. A layer of monomers below that layer is then less uniform and the alternating zones of varying density of monomers continues into the film to the point where the density becomes equivalent to the bulk. Those bound by two smooth repulsive walls gives rise to monomer mobility increasing upon approach to the smooth interface thus reducing the glass transition temperature of the film.

When there is molecular level structure in the surface wall there is localisation of monomers even for weak interactions. The crystalline properties of the wall induce symmetry resembling the crystalline structure. This reduces molecular mobility. When reviewing the effects of attractive interactions from smooth walls [73, 74] the polymers exhibit different dynamical properties. Layer-by-layer analysis of a coarse-grained model simulation, for copolymers with constant density, between two attractive substrates revealed that the monomers near the smooth surface always had lower segmental mobility which decreased as the wall attraction increased. The simulation results also revealed that, as the wall attraction is increased, the monomers in the film interior become more mobile. The higher attraction promotes increased order at the surface thus reducing molecular mobility, this then promotes less order within the sample thus explaining the increase in molecular mobility within the interior.

As seen in section 2.2.2, there is a connection between the glass transition and free volume, the link has been revisited consistently in recent times. White and Lipson produce an extensive review this topic and forms the foundations of our discussion [75]. We now define free volume in order to give an insight into why it is so important leading up to and during vitrification. Rearranging equation 2.7 we can define free volume as the total volume of the glass-forming substance less a measure of “occupied”/”hard-core” volume. The main difference between the theories and what leads to such a wide variety of results, is how the researchers define the hard-core volume.

The first case would be to define it as an occupied volume, V_{oc}, as done in the locally correlated lattice (LCL) theory. Another side note would be the authors of [75] have a vested interest in the LCL model therefore the advantages of this are highlighted quite often. The second, the occupied volume, considers free volume to be made of two parts: vibrational free volume, $V_{\mathrm{f:vib}}$, and excess free volume, $V_{\mathrm{f:exs}}$.

- Vibrational free volume
  - Free space contained within the temperature dependent free volume.
  - The vibrational volume, V_{vib}, can be thought of as a combination of the vibrational free volume and the hard-core volume – the hypothetical volume that segments would possess in crystalline form.
    - This can be referred to as occupied volume [76-78].
- Excess free volume – this is the additional free volume needed to give the overall amount in possession by the melt.

The different free volume contributions, occupied volume and vibrational volume can be seen in figure 2.10.

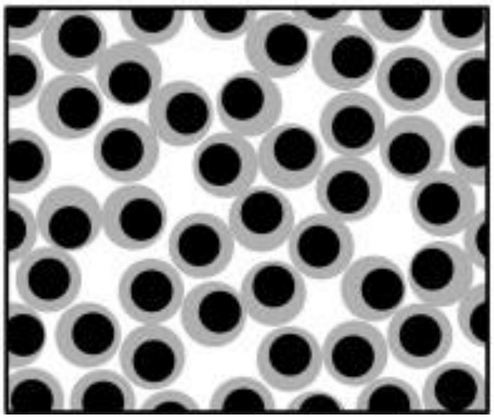

$V_{\mathrm{f}} =$ white + grey

$V_{\mathrm{oc}} =$ black $V_{\mathrm{f:exs}} =$ white

$V_{\mathrm{vib}} =$ black + grey $V_{\mathrm{f:vib}} =$ grey

Figure 2.10: Conceptualisation of free volume within a liquid. Reprinted (adapted) with permission from R. P. White and J. E. G. Lipson. Polymer free volume and its connection to the glass transition. *Macromolecules*. **49** 3987–4007, 2016. Copyright 2017 American Chemical Society. Black circles are the hard-core volume of the liquid particles. The encasing grey is the vibrational free volume that the particles can move in if they were to vibrate about their equilibrium positions as in a solid. The remaining white space is the excess free volume available to the liquid particles to move through.

The excess free volume, as in figure 2.10, allows the liquid particles to rearrange around their neighbours. There is a conceptual understanding of what the vibrational and excess free volume are [79]. With the case of vibrational free volume – as temperature increases, the free space around each particles expands, the distance to their nearest neighbours increases while the number of neighbours remains the same. For excess – the distance to nearest neighbour remains fixed while the number decreases. For a liquid, both types of expansion occur whilst for a solid only the vibrational expansion occurs. The excess free volume is most difficult to determine quantitatively and it is this that varies so much amongst earlier works.

If we accept the correlation between T_g and free volume, we can define the glass transition as being when the free volume of polymers drops below a threshold value. For the case of polymer thin films, free volume can be increased at surfaces. Two pieces of research have opposing ideas of how the free volume increases at the surface. One idea, as suggested by de Gennes [13, 80-81], is that free volume diffuses into the polymer sample via kinks along the polymer chains, related to the polymer conformations, at the free surfaces. At the kink, the free volume propagates a finite depth into the sample along the chain backbone – implying a molecular weight dependence as longer chains will allow free volume to diffuse deeper below the free surface. There is a competition between two types of motion: one associated with short range rearrangements (normally associated with bulk T_g) and the other concerns “sliding motion” where the chain diffuses via mobile kinks at the free surface where there is a larger free volume available. This allows for faster structural relaxation and explains the reduction in local T_g.

However, in 2011, research disagreed with the above theory [82]. The distribution of glass transition temperatures in free-standing, nanoconfined PS thin polystyrene films were considered. Using a relatively new technique that uses self-referencing fluorescence to measure T_g values within surface and interior layers of known thickness, it is demonstrated via trilayer films (the middle layer is pyrene-labeled PS, with surrounding films as neat PS) that there is a reduction in T_g in the middle layer where chains are unable to form the necessary kinks as described by de Gennes. This phenomenon is instead attributed to the strongly perturbed cooperative dynamics present in the middle layer due to the size of the surrounding neat PS layers.

Thus far, there has been a great deal of discussion on what affects the glass transition temperature. We’ve discussed the effects of confinement and free volume. As alluded to and briefly mentioned in references and the introduction, a mobile surface layer seems to exist on top of nanoconfined thin polymer films which gives rise to a distribution of glass transition temperatures throughout the sample. We shall now give a brief overview of the literature that suggests this and those that offer potential origins.

Proof of the mobile surface layer and the depth at which it exhibits an effect is found to be 10 nm [83] which is consistent with future literature. Via continuous measurement using ellipsometry the changing film thickness as temperature increased and they also measured for decreasing temperature, too. They ensured there was no thermal damage by increase the temperature to well above the glass transition temperature, observing no effect with the ellipsometric angle. It was Ellison and Torkelson [14] who provided the first piece of evidence, experimentally, that there was a distribution of T_g. Using a fluorescence method, it was established that a mobile surface layer as defined by its enhanced dynamics permeates several tens of nanometres into the film [82]. They used the fluorescent probe in parallel to the substrate within layers of pure polymers. They found there was indeed a gradient of T_{g} in the film.

There have been further direct measurements of the liquid-like more mobile surface layer [84]. The usual PS thin films were used, they were given a high surface coverage of nanodeformations by partially embedding and removing gold nanospheres up to 4 nm into the surface. They measured the time-dependent relaxation of the deformations as a function of temperature. Surface relaxation was observed for all temperatures implying enhanced surface mobility. The gold spheres are dissolved into a mercury droplet ensuring no extra stress is applied during the removal. X-ray analysis was carried out to ensure no gold or mercury residue remained. They used AFM to monitor the size of the holes, this inherently presents its own problems even with the authors stating they used a sharp tip to overcome radius of curvature issues and the frequent changing of the tip.

More recently, via simulations for PMMA thin films, a comparison between low and high molecular weight films shows there is a link between the amount of free volume present at a free surface and the mobile surface layer [85]. This model has the advantage of being parametrised from previous atomistic simulations such that the local structure and thermomechanical properties are accounted for. The reduced interfacial density at the free surface in low molar mass films leads to an increase in local free volume at the free surface thus producing a greater reduction in glass transition temperature. This can be attributed to an enhancement of segmental mobility, evidence of a mobile surface layer.

The surface diffusion of molecules, that have moderate perturbation of surfaces, is decoupled from the enhanced surface dynamics and depression of glass transition temperature with a specific polymer glass [86]. This is quite counterintuitive, although there is a heightened surface diffusion in comparison to the bulk, as the film thickness decreases from 400 to 12 nm, relaxation dynamics increase and the expectation would be that the surface diffusion would also increase in tandem with the relaxation dynamics but this is not the case. Ultrathin films of N,N'-bis(3-methylphenyl)-N,N'-diphenylbenzidine (TPD) polymer on top of silicon substrates were used to resemble the typical thicknesses in organic electronics and coatings that are less than one hundred nanometres. A tobacco mosaic virus (TMV)-probe was the diffusing particle and its temporal surface tension-driven flow was monitored via AFM. Wetting experiments were used to monitor the effective viscosity which gives a measure of the dynamics of the films. It is proposed that the surface diffusion is discrete and completely decoupled from both surface and bulk dynamics. The rationale behind this is that the surface diffusion could be correlated to surface dynamics (relaxation time of the surface) instead of the glass transition temperature which is average film dynamics, since this is also insensitive to film thickness. A key point here is that heightened surface diffusion has been exhibited but the demonstrated process as to how remains unclear.

CHAPTER 3: Experimental Techniques

The main techniques used in this research were Ellipsometry for the determination of the glass transition temperature and Fluorescence Correlation Spectroscopy (FCS) for the single molecule diffusion. DOSY NMR is used to measure 3D diffusion of rhodamine-B PEG but as it was not a main dedicated piece of work, it is briefly introduced.

3.1 Ellipsometry

To determine the glass transition temperature of a sample, the length scale and the properties of the sample need to be considered. For the case of thin films, a nanometre length scale and thus we become increasingly limited by our experimental capabilities when using commonplace optical instruments. There are several approaches to measure the thermal properties of the sample, such as expansivity, and to examine how these properties change in response to temperature. A non-invasive approach that can peer through the entirety of thin samples, using reflection, is ellipsometry.

The disadvantages of using reflection techniques are the reliance of modelling, the parameters measured are determined indirectly and the sample must be transparent such that the incident wave is able to propagate through the sample and be detected. By reviewing the properties of light and how light propagates through media the measurable parameters required for ellipsometry can be derived.

3.1.1 Properties of light: a review

Firstly, to understand how the reflection of light can infer physical properties, prior knowledge of light, its mathematical formulae and physical behaviour, and how light interacts with matter must be addressed. Consider the wave-like properties of light which describes light as two cosinusoidal, orthogonal waves that are both orthogonal to the direction of their propagation. The two waves are the electric, $\mathbf{E}$, and magnetic fields, $\mathbf{B}$, and are defined as:

$$E_x(z,t) = E_{0x}\cos\left[\omega\left(t-\frac{z}{c}\right)+\phi\right] \tag{3.1}$$

and

$$B_y(z,t) = \frac{B_{0y}}{c}\cos\left[\omega\left(t-\frac{z}{c}\right)+\phi\right], \tag{3.2}$$

where E_{0x} and B_{0y} are the respective electric and magnetic field amplitudes, ω is the angular frequency of the wave, c is the speed of light, ϕ is the phase shift and the waves are deemed to propagate along the z-axis. The electric and magnetic fields will always be orthogonal to each other so for the following discussion the electric field shall only be discussed but will also apply to the magnetic field.

The electric wave propagating along the z-axis can be split into vector components, $\hat{\mathbf{i}}$ and $\hat{\mathbf{j}}$, that act in the x- and y-axes, respectively. Each component can mathematically be written as:

$$\mathbf{E}_x(z,t) = \hat{\mathbf{i}}E_{0x}\cos(kz - \omega t) \tag{3.3}$$

and

$$\mathbf{E}_y(z,t) = \hat{\mathbf{j}}E_{0y}\cos(kz - \omega t + \phi) \tag{3.4}$$

where k is the wavenumber ($k = \frac{2\pi}{\lambda}$), E_{0x} and E_{0y} are the amplitude of the electric field x and y vector components, respectively and all other terms are as defined previously. Thus, the resultant electric field vector is the summation of the two vector components and can be expressed as

$$\mathbf{E} = \mathbf{E}_x + \mathbf{E}_y = \hat{\mathbf{i}}E_{0x}\cos(kz - \omega t) + \hat{\mathbf{j}}E_{0y}\cos(kz - \omega t + \phi). \tag{3.5}$$

The dissection of the electric wave into vectors allows for interesting phenomena to be observed and exploited for experimental gain. By changing the values of E_{0x}, E_{0y} and ϕ different polarisations can be established.

Linear polarisation: $\phi = 0, \pm n\pi$ (n is any integer)

- Both component waves are in phase and corresponding maximum occur simultaneously in time along the axis of propagation. Traces out a linear plot.

Circular polarisation: $\phi = \pm\frac{m\pi}{2}$, $E_{0x} = E_{0y}$ (m is any odd integer)

- Both waves are 90° out of phase and one component wave's maximum corresponds to the other's zero contribution. The resultant $\mathbf{E}$ traces out a circular path in the axis of propagation.

Elliptical polarisation: $\phi = \pm\frac{m\pi}{2}, E_{0x} \neq E_{0y}$ (m is any odd integer)

- Both waves are 90° out of phase and now the component waves have maximum amplitudes that are not equal. This creates a semi-major axis always along the axis of the component with the larger amplitude. This is the form of polarisation that is used in ellipsometry.

All other cases: $\phi = \pm\frac{n\pi}{2}$ (n is any integer)

- Resultant vector traces out an elliptical path but the angles between cartesian and elliptical axes are not necessarily multiples of $\frac{\pi}{2}$.

3.1.2 Light incident at interfaces

Whilst light can be manipulated to produce different polarisations, how it interacts with matter and interfaces will determine what data a technique can achieve. It is useful to review how light behaves when incident on an interface. At an interface between media of different refractive index, light can either be reflected or refracted whilst undergoing transmission (the simplest case is illustrated in figure 3.1). In the case of reflection, light follows the law of reflection such that

$$\theta_i = \theta_r \tag{3.6}$$

and for transmission, light obeys Snell's law as defined by

$$n_i \sin\theta_i = n_t \sin\theta_t \tag{3.7}$$

where θ is the angle at which the light is incident, reflected or transmitted with respect to the normal, n is the refractive index of the medium and the subscripts i, r and t represent the incident, reflected and transmitted light, respectively.

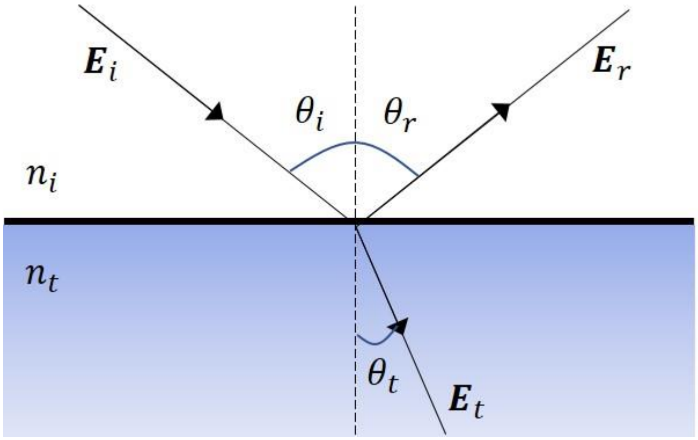

Figure 3.1: A visualisation of the electric field incident on a boundary between two media of different refractive index. The vertical dashed line represents the plane of incidence, the thick horizontal line is the boundary between the two media, n_i and n_t are the refractive indicies of the medium that the electric wave is incident and the medium that the electric wave is transmitted through, respectively.

For the purposes of resolving electromagnetic waves into their vector components, a set of axes must be defined. In the case of interfaces, these axes are defined as along the place of incidence and perpendicular to said plane. Due to the electromagnetic field consisting of two orthogonal waves, each component will correspond to one of the defined axes. Moreover, along the boundary the following continuity between electric field vectors applies

$$\mathbf{E}_i + \mathbf{E}_r = \mathbf{E}_t. \tag{3.8}$$

For the electromagnetic field component that is perpendicular to the plane of incidence, the individual components can be expressed in terms of the associated angles

$$n_i(E_{0i} - E_{0\mathrm{r}})\cos\theta_i = n_t E_{0\mathrm{t}} \cos\theta_t\,. \tag{3.9}$$

Via substitution of equation 3.8 into 3.9 this yields the amplitude reflection coefficients, $r_{\perp}$, and rearranging E_t in terms of E_i and substitution into the above yields the amplitude transmission coefficient, $t_{\perp}$, both amplitude coefficients are defined

$$r_{\perp} = \left(\frac{E_{0r}}{E_{0i}}\right)_{\perp} = \frac{n_i \cos\theta_i - n_t \cos\theta_t}{n_i \cos\theta_i + n_t \cos\theta_t} \tag{3.10}$$

and

$$t_{\perp} = \left(\frac{E_{0t}}{E_{0i}}\right)_{\perp} = \frac{2n_i \cos\theta_i}{n_i \cos\theta_i + n_t \cos\theta_t}. \tag{3.11}$$

For the electric field component that is parallel to the plane of incidence, following a similar treatment to the above the following amplitude reflection and transmission coefficients are found

$$r_{||} = \left(\frac{E_{0r}}{E_{0i}}\right)_{||} = \frac{n_t \cos\theta_i - n_i \cos\theta_t}{n_i \cos\theta_t + n_t \cos\theta_i} \tag{3.12}$$

and

$$t_{||} = \left(\frac{E_{0t}}{E_{0i}}\right)_{||} = \frac{2n_i \cos\theta_i}{n_i \cos\theta_t + n_t \cos\theta_i}. \tag{3.13}$$

Equations 3.10 to 3.13 are the Fresnel equations [89] and apply only to isotropic, linear and homogenous media. It is with these equations that the useable information from reflectance in ellipsometry can be measured. A complex reflection ratio, ρ, which details the changes in phase shift and amplitude upon reflection is given by

$$\rho = \frac{r_{||}}{t_{\perp}} = \tan\Psi \mathrm{e}^{i\Delta} \tag{3.14}$$

where Ψ and Δ are the ellipsometric parameters that are measured in an ellipsometry experiment.

3.1.3 Reflection and transmission in thin films

So far, a simple approach that only considers the reflection and transmission of electromagnetic fields between two media allowed for the derivation of a relation containing the ellipsometric parameters. For thin films, there is an added level of complexity because the light waves are not only reflected and transmitted into the sample but some of the transmitted light is then reflected from the substrate that the thin film is bound to (see figure 3.2). This reflected light from the substrate is then transmitted through the thin film and is combined with the initial reflected light that is detected. Another consideration is that this can occur multiple times throughout the sample.

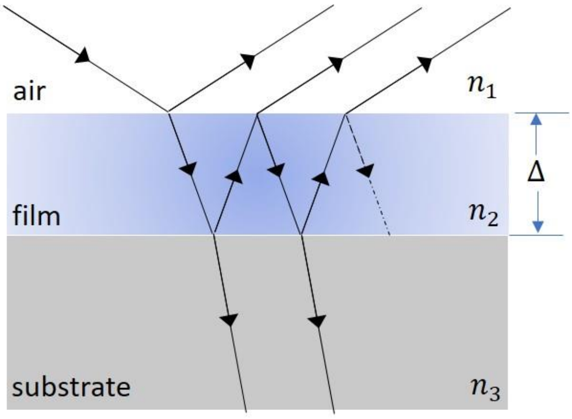

Figure 3.2: Ray paths of electromagnetic waves passing through several media showing the different reflection and transmissions at the media boundaries. The example used corresponds to a film, of thickness Δ, deposited on a substrate.

The total amplitude reflection coefficient can be derived in a similar fashion to the individual reflection coefficient. A light wave with initial amplitude A is incident on a boundary between the incident medium, with refractive index n_1, and the first transmission medium, with refractive index n_2. This first transmission medium is the film of thickness Δ. The light wave will then incident on the next boundary between the film and the substrate with refractive index n_3 where the substrate surface is considered to have infinite depth where the light that is transmitted is no longer measurable. It is assumed that $n_1 < n_2 < n_3$.

In section 3.1.2, the wave that is incident at the boundary between air and film is identical to the current scenario where reflection from the air-film interface occurs. Therefore, the new amplitude of this wave is Ar_{12} where 1-2 indicates passing from incident to film and so on. Withal, further contributions from the waves that have been reflected from the film-substrate, 2-3, that then leave through the 2-1 interface. Transmitting through the film results in the wave to now undergo a phase shift equal to

$$\exp(-ik_z\Delta) = \exp\left(-\frac{i2\pi n_2 \cos\theta_2\,\Delta}{\lambda}\right) = \exp(-i\delta_2), \tag{3.15}$$

where

$$\delta_2 = \frac{2\pi n_2 \Delta \cos\theta_2}{\lambda}, \tag{3.16}$$

k_z is the wavenumber and λ is the wavelength of the phase shifted light. The modified amplitude of the transmitted wave that reaches the 2-3 interface is given by the product of the 1-2 transmission coefficient t_{12}, the original wave amplitude A and the phase shift applied to the wave as it transmits through the film

$$At_{12}e^{-i\delta_2}. \tag{3.17}$$

Some of the wave is then reflected back from the 2-3 interface with modified amplitude

$$A t_{12} e^{-i\delta_2} r_{23}\,, \tag{3.18}$$

which now contains a factor of r_{23}, the reflection coefficient of the 2-3 interface. This reflected light then passes through the 2-1 interface and is detected by the measuring equipment with a modified amplitude equal to

$$A\, t_{12}\, e^{-i\delta_2}\, r_{23}\, e^{-i\delta_2}\, t_{21}\,. \tag{3.19}$$

Since the light propagates through the film a second time, after reflection at the 2-3 interface, there is a second phase shift and another transmission factor from the 2-1 interface, t_{21}.

Following the same methodology for further reflections between interfaces 1 and 3, the total amplitude detected can be expressed as

$$A\left(r_{12} + t_{12}\, e^{-i\delta_2}\, r_{23}\, e^{-i\delta_2}\, t_{21} + t_{12}\, e^{-i\delta_2}\, r_{23}\, e^{-i\delta_2}\, r_{21}\, e^{-i\delta_2}\, r_{23}\, e^{-i\delta_2}\, t_{21} + \cdots\right). \tag{3.20}$$

Therefore, the total reflection coefficient, R_{total}, is given by

$$R_{\text{total}} = r_{12} + t_{12}\, r_{23}\, t_{21}\, e^{-2i\delta_2}\left[1 + \, r_{21}\, r_{23}\, e^{-2i\delta_2} + \left(r_{21}\, r_{23}\, e^{-2i\delta_2}\right)^2 + \cdots\right] \tag{3.21}$$

There is potentially an infinite number of reflections and equation 3.21 must converge. Recall the series expansion for an infinite series,

$$\sum_{i=0}^{\infty} x^i = 1 + x + x^2 + x^3 + \cdots = \frac{1}{1-x} \quad \text{where } x \ll 1. \tag{3.22}$$

Combining this with the following relations derived from equations 3.10-3.13 (the Fresnel equations),

$$r_{12} = -r_{21} \tag{3.23}$$

$$t_{12} t_{21} = 1 - r_{12}^2, \tag{3.24}$$

the total reflection coefficient is defined as:

$$R_{\text{total}} = \frac{r_{12} + r_{23}\exp(-2i\delta_2)}{1 + r_{12}\, r_{23}\exp(-2i\delta_2)}\,. \tag{3.25}$$

The effect of polarisation is addressed by substituting in the corresponding Fresnel equations into equation 3.25. Light polarised perpendicular and parallel to the plane of incidence requires the substitution of equation 3.10, $r_{\perp}$ and equation 3.12, $r_{||}$, into equation 3.25, respectively.

Measurement of reflection data from a sample of a thin film, the data is fitted to the total reflection coefficient, R_{total}, with the polarisation equations substituted in. This equation has the film thickness, Δ, in the phase shift parameter, δ_2, so the experimental data yields the film thickness that can then be used to infer when the thin film has undergone a glass transition and thus the glass transition temperature.

3.2 Fluorescence Correlation Spectroscopy

Whilst ellipsometry is able to use reflectivity to delve into the physical structure of the sample at the nanometre scale, in the case of thin films, an even greater challenge is present when constructing an experimental setup to measure dynamical data of single molecules. A series of techniques has been devised to accomplish this task and although imaging these molecules remains quite difficult, obtaining quantifiable data that produces a well-defined view of the system can be accomplished. One of those techniques, specifically for single molecules, is fluorescence correlation spectroscopy (FCS). Alternative techniques are discussed in section 3.2.4.

Fluorescence correlation spectroscopy measures small fluctuations in intensity of fluorescence with respect to an initial intensity at a defined starting time. It was an evolution of dynamic light scattering for smaller scale molecules [90, 91]. Dynamic light scattering is used primarily to measure the size of molecules suspended in a liquid by scattering light to monitor their Brownian motion. The FCS technique was originally applied to observing DNA-drug interactions [91, 92], however, the main issue with this first experiment was the poor signal-to-noise ratio. The detection volume produced relatively small fluctuations in intensity in comparison to the excessive emission from the surrounding medium of the focal point.

Twenty years later, a modification to the FCS technique was introduced, to remove the background noise confocal microscopy was combined with FCS [93]. The detection volume was reduced below 1 femtolitre such that signal molecules in solution could now be detected and low concentration solutions, of order picomolar (pM) and nanomolar (nM), could be used [94]. Due to it being non-invasive, FCS continues to be used in a variety of ways such as developing our understanding of calcium cell-signalling by monitoring the free diffusion coefficients in the ions binding process [95], measuring the change in effective hydrodynamic radius of polymer-coated nanoparticles adsorbing to proteins [96] and in observing phase transition effects, or lack thereof, in live cell plasma membranes [97].

An AxioVert inverted confocal microscope with a Zeiss ConfoCor2 FCS module was used to perform all FCS experiments for this work.

3.2.1 Confocal Microscopy

In general, to create an image in microscopy an assortment of optics focusses light from a specific point within a sample onto a detector. The detector then uses this light to create an image or produce a measurement of intensity of the light detected. Ideally, all the photons from the region of interest are detected and no background noise. What occurs in a real system is the planes other than the focal plane within the sample produce additional signal, background noise, that will contribute to the measured intensity producing a misrepresentation of the sample of interest. At the single molecule level, the intensity of the noise is more problematic as it is comparable to the signal of the single molecule itself.

To refine the measured signal, removing the background noise and improving the signal-to-noise ratio, Marvin Minsky patented a novel confocal technique that introduced a series of pinholes into the system that reduced the amount of off-focal plane photons that are detected [98, 99]. This method ensures that only the light emitted from the focal point, the sample of interest, is focussed at the detector by allowing the photons through the pinhole and bringing the off-focal plane light to a focus before or after the pinhole as seen in figure 3.3. The pinhole is moved until the intensity from the focal point is at maximum. The pinhole is therefore *con*jugated to the *focal* plane.

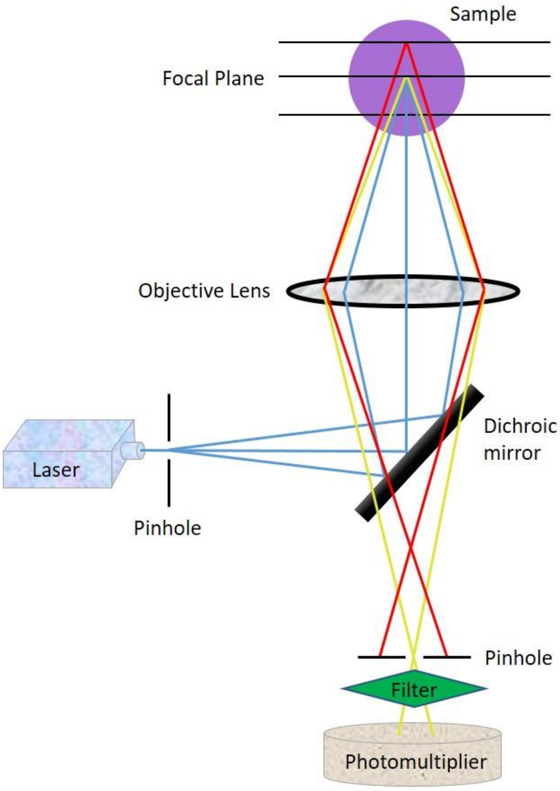

Figure 3.3: Simplified diagram of a basic FCS setup. A laser emits monochromatic light (blue line) at a specific wavelength tuned to the wavelength of the sample tagged with a fluorescent molecule. The dichroic mirror only allows emitted light that has been shifted in wavelength by a sufficient amount. Remitted photons from the focal point (yellow line), from the sample of interest, can pass through the pinhole and can focus on the detector. Off-focal photons from the background (red line) are blocked by the pinhole.

The resolution limits of confocal microscopy have slight advantages over regular far field view microscopy. The $x - y$ resolution is determined by the following equations; the left-hand side represents the far field view and the right-hand side equation is the confocal microscopy resolution limit.

$$r = \frac{0.61\lambda}{NA} \qquad \text{and} \qquad r = \frac{0.4\lambda}{NA} \quad ,$$

where r is the minimum distance two points can be distinguished, λ is the wavelength of light used and NA is the numerical aperture of the objective. For this work an objective with numerical aperture equal to 1.2 and a laser wavelength of 543 nm would produce a resolution limit of 0.28 μm for wide field regular microscopy but with confocal microscopy this limit is improved to 0.18 μm. Similarly, the z-axis resolution limit is defined in a similar way but there is now a quadratic dependence on numerical aperture:

$$r = \frac{2\lambda}{NA^2} \qquad \text{and} \qquad r = \frac{1.4\lambda}{NA^2} \quad .$$

For this work, wide field would allow a resolution limit in the z-axis of 0.75 μm and confocal microscopy has 0.53 μm resolution limit.

3.2.2 The theory of FCS

A laser will illuminate a specific volume of the sample, termed the 'confocal volume'. The laser will emit the corresponding excitation energy photons with their required wavelength by the fluorescent molecule that is associated with the sample of interest. When the fluorescent molecule relaxes, from its higher energy state, it will reemit a photon at a longer wavelength which will be detected by the photomultiplier.

The light is then filtered out and the time in which the molecule fluoresces within the confocal volume corresponds to the duration of increased intensity. Therefore, put simply, FCS is used to measure the amount of time a molecule requires to move through a defined volume. As the molecules within the sample will be continuously diffusing, there will be a limited number of molecules, with one being the desired amount, diffusing through the confocal volume thus the time taken for very few molecules to fluoresce can be measured.

There are several different ways a molecule can diffuse through the detection volume as depicted in figure 3.4. In the ideal case, the detection volume is a hard sphere of radius, *R*. The diffusing molecule would pass through the confocal volume straight through the centre of the sphere.

In the ideal diffusion case, at a time t the molecule will enter the detection volume, it will be excited by a photon at the appropriate energy and lead to an increase in intensity. This intensity will continue for all of time $t + \tau$. Once the molecule reaches the end of the sphere diameter ($2R$), the molecule will stop fluorescing and the intensity will drop down to its original level. The time it takes for the molecule to diffuse, τ_{D}, the 'diffusion time', is the total time the intensity increases (see figure 3.5).

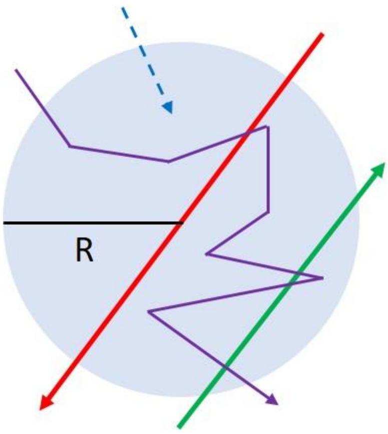

Figure 3.4: For a given confocal volume there are several potential diffusion paths that a fluorescent molecule can take. The ideal case, the red arrow, is the molecule passes directly through the centre of the hard sphere of radius, R, which is also the assumed ideal confocal volume. The other cases that do occur in real systems, are the shorter paths that do not pass through the centre (green), there are the longer paths that do not diffuse in a straight line and follow a haphazard direction (purple) via thermal fluctuations and collisions. There is also a fourth case that will be discussed further in section 3.2.3 which is the dashed blue arrow representing a molecule entering the triplet state and no longer fluorescing.

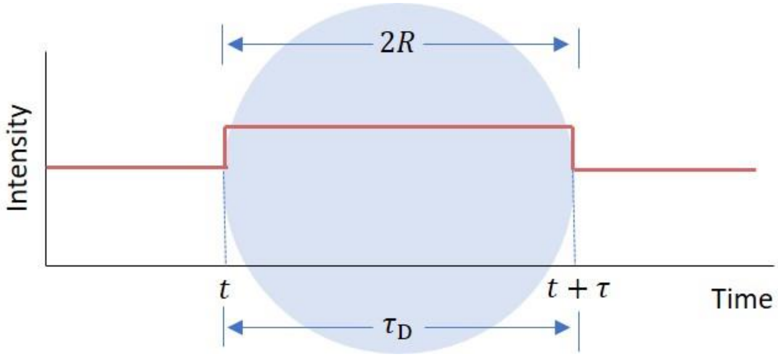

Figure 3.5: An ideal intensity profile as a function of time for a fluorescing molecule that diffuses directly through the centre of a spherical confocal volume of well-defined diameter, $2R$.

In order to better model and interpret the experimental results, the simplistic and ideal assumptions must now be developed to represent a real system. There are several assumptions made thus far that can be addressed and will act to either increase or decrease the diffusion time. Firstly, mentioned previously, the diffusing molecule can take a shorter route or indirect route through the confocal volume leading to a shorter or longer diffusion time, respectively. Secondly, the diffusion time will depend on the speed at which molecules pass through the confocal volume and not all molecules will have the same speed. There will be a distribution of speeds due to a distribution of thermal energy about an average value. Finally, the confocal volume itself is not a hard sphere of well-defined radius R. The "boundary" is defined by a decrease in light intensity and the convention is to use whenever the intensity drops by a factor of e. The light intensity does not decrease isotropically as it is different in the (x, y) plane compared to the (z) plane. The shape of this confocal volume is similar to an elongated "rice grain" (see figure 3.6) and is mathematically defined as

$$I\ (x, y, z) = I_0 \exp\left(-2\frac{x^2 + y^2}{\omega_{\mathrm{xy}}^2}\right) \exp\left(-2\frac{z^2}{\omega_{\mathrm{z}}^2}\right), \tag{3.26}$$

where I_0 is a constant, ω_{xy} is the beam decay waist in the (x, y) plane and ω_{z} is the corresponding beam decay height along the z axis.

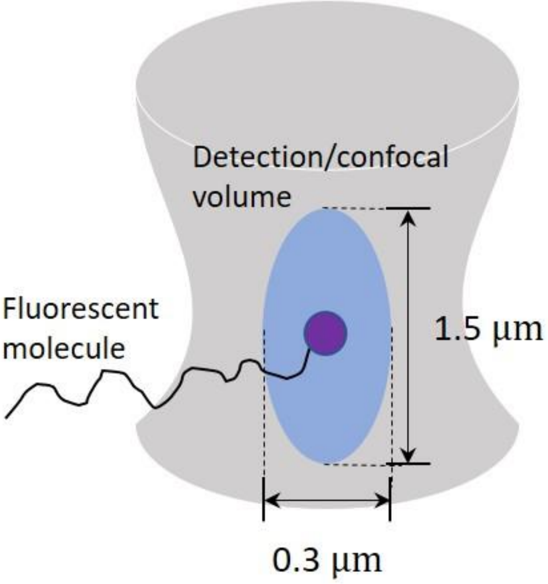

Figure 3.6: A representation of the elongated rice grain confocal volume (blue ellipse). A fluorescent tag (purple circle) on the molecule (black curly line) passes through the confocal volume and is illuminated. The surrounding medium is the rest of the sample (grey). The size of the rice grain is determined from precisely controlled experiments.

3.2.3 The autocorrelation curve

The diffusion times of the fluorescent molecules are determined from the change in photon intensity they produce. This sets the mathematical framework for how to extrapolate the diffusion times, the self-similarity of the intensity profile about the average intensity over the whole measurement of the intensity profile must be examined. The derivation of the autocorrelation equation is found in the original works and more modern interpretations [100].

Firstly, to determine the self-similarity, the change in intensity must first be defined. This is the intensity at any given moment $I\ (t)$ compared with the average intensity $\langle I\ (t)\rangle$

$$\delta I\ (t) = I\ (t) - \langle I\ (t)\rangle, \tag{3.27}$$

where $\langle I\ (t)\rangle$ is the temporal average of the duration of the measurement t_{total}

$$\langle I\ (t)\rangle = \frac{1}{t_{\text{total}}}\int_{0}^{t_{\text{total}}} I\ (t)\ \mathrm{d}t\ \cdot \tag{3.28}$$

Assuming the fluctuations in intensity are a result of chan ges in local concentration, δC, in the effective confocal volume, V_{eff}, then the intensity fluctuation can be expressed using the efficiency of the experimental setup with the probability of exciting a fluorescent molecule:

$$\delta I\ (t) = \kappa \int_{V_{\text{eff}}} I_{\text{ex}}\,(\boldsymbol{r})\ \cdot\ S\ (\boldsymbol{r})\ \cdot\ \delta\left(\sigma \cdot q \cdot C\ (\boldsymbol{r},t)\right)\ \cdot\ \mathrm{d}V, \tag{3.29}$$

where κ is the detection efficiency of the reemitted photons, $I_{\text{ex}}(\boldsymbol{r})$ is the excitation energy distribution within the confocal volume, $S(\boldsymbol{r})$ determines the collection efficiency of the experimental setup (*optical transfer function*), σ is the molecular absorption of photons cross-section, q is the fluorescence quantum yield and $C(\underline{r},t)$ spatial and temporal molecular concentration.

It is quite difficult to determine the individual parameters in equation 3.29 and some simplification of the equation, informed from the system, can aid the analysis. Firstly, the detection efficiency, excitation intensity, molecular absorption cross-section and fluorescence quantum yield can be combined to give a photon count per molecule per second relation, denoted by η_0, i.e.

$$\eta_0 = \ I_0 \cdot \kappa\ \cdot q\ \cdot \sigma\ . \tag{3.30}$$

We can combine two optical transfer functions into one spatial term, denoted as $W\ (\underline{r})$ and defined as

$$W\ (\boldsymbol{r}) = \frac{I_{\text{ex}}\,(\boldsymbol{r})}{I_0} \cdot S\ (\boldsymbol{r})\ \cdot \tag{3.31}$$

It can be assumed that the spatial distribution takes on a three-dimensional Gaussian distribution, thus equation W can take on the form of equation $I(x, y, z)$ (equation 3.26). Moreover, equation 3.3 (δI) can be rewritten as:

$$\delta I\ (t) = \int_{V_{\text{eff}}} W\ (\boldsymbol{r})\, \delta\big(\eta\ \cdot\ C\ (\boldsymbol{r},t)\big)\ \cdot \mathrm{d}V\,. \tag{3.32}$$

Now the change in fluorescence in the confocal volume has been defined, the self-similarity between times t and $t + \tau$ are analysed by an autocorrelation function, $G(\tau)$, which is normalised with respect to the average intensity

$$G\ (\tau) = \frac{\langle \delta I\ (t)\ \cdot \delta I\ (t+\tau)\rangle}{\langle I\rangle^2}, \tag{3.33}$$

where τ is the total time for which the measurement is taken over. The autocorrelation function determines the fluctuations in intensity within the effective detection volume V_{eff}. The next step is to substitute equation δI (equation 3.32) into the autocorrelation function (equation 3.33) yielding the following expression

$$. \tag{3.34}$$

$$G\ (t,\tau)=\frac{\iint W\ (\boldsymbol{r})\ W\ (\boldsymbol{r}')\ \langle\delta\left(\eta\ \cdot\ C\ (\boldsymbol{r},t)\right)\delta\left(\eta\ \cdot\ C\ (\boldsymbol{r},t+\tau)\right)\rangle\ \mathrm{d}V\mathrm{d}V'}{\left(\int W\ (\boldsymbol{r})\ \langle\delta(\eta\ \cdot\ C(\boldsymbol{r},t))\rangle\ \mathrm{d}V\right)^2}$$

Expressing the fluctuation term as

$$\delta\left(\eta\ \cdot\ C\ (\boldsymbol{r},t)\right)=C\delta\eta+\eta\delta C \tag{3.35}$$

and assuming that the molecule's fluorescence properties will not change during the measurement time implies that $\delta\eta=0$. Therefore, the autocorrelation function is defined as

$$G\ (t)=\frac{\iint W\ (\boldsymbol{r})\ W\ (\boldsymbol{r}')\ \langle\delta C(\boldsymbol{r},0)\ \ \delta C(\boldsymbol{r},\tau)\rangle\ \mathrm{d}V\mathrm{d}V'}{(\langle C\rangle\int W\ (\boldsymbol{r})\ \mathrm{d}V)^2}\,. \tag{3.36}$$

The type of diffusion, whether it is free three-dimensional diffusion or anisotropic surface two-dimensional diffusion, will result in two different expressions tailored to the individual situation.

Free diffusion:

Taking the spatial term, $W\ (\boldsymbol{r})$ (equation 3.31), to be the shape of confocal volume, $I\ (x,y,z)$ (equation 3.26), and the number density autocorrelation term, $\langle\delta C\ (\boldsymbol{r},0)\ \ \delta C\ (\boldsymbol{r}',\tau)\rangle$, becomes

$$\langle\delta C\ (\boldsymbol{r},0)\ \ \delta C\ (\boldsymbol{r}',\tau)\rangle=\langle C\rangle\frac{1}{(4\pi D\tau)^{-\frac{3}{2}}}\exp\left[-\frac{(\boldsymbol{r}-\boldsymbol{r}')^2}{4D\tau}\right]. \tag{3.37}$$

Using equation 2.5, the diffusion coefficient, D, is expressed as:

$$D=\frac{\omega_{\mathrm{xy}}^2}{4\tau_{\mathrm{D}}}, \tag{3.38}$$

where ω_{xy}, the beam waist, is the distance travelled by the diffusing particle (x in equation 2.5). Substituting the above number density autocorrelation function (equation 3.37) and the diffusion coefficient into the autocorrelation function equation (equation 3.36) this yields:

$$G_{\mathrm{3D}}=\frac{1}{V_{\mathrm{eff}}\ \langle C\rangle}\frac{1}{\left(1+\frac{\tau}{\tau_{\mathrm{3D}}}\right)}\frac{1}{\sqrt{1+\frac{\tau}{\Gamma^2\tau_{\mathrm{3D}}}}}, \tag{3.39}$$

where τ_{3D} is the free three-dimensional diffusion time, $\langle C\rangle$ is the average concentration in the confocal volume, V_{eff} is the effective confocal/detection volume and is expressed as

$$V_{\mathrm{eff}}=\frac{\left(\int W\ (\underline{r})\ \mathrm{d}V\right)^2}{\int W^2\ (\underline{r})\ \mathrm{d}V} \tag{3.40}$$

and the structural parameter, Γ, is defined as

$$\Gamma=\frac{\omega_{\mathrm{z}}}{\omega_{\mathrm{xy}}}\,. \tag{3.41}$$

Surface diffusion:

For two-dimensional surface diffusion, it is assumed the molecules move in the (x, y) plane only therefore the z-component contributions can be ignored. Following the same methodology as for free three-dimensional diffusion, the following autocorrelation function is found

$$G_{2\mathrm{D}} = \frac{1}{V_{\mathrm{eff}} \langle C \rangle} \frac{1}{\sqrt{\left(1 + \frac{\tau}{\tau_{2\mathrm{D}_\mathrm{x}}}\right)\left(1 + \frac{\tau}{\tau_{2\mathrm{D}_\mathrm{y}}}\right)}}, \tag{3.42}$$

where V_{eff}, $\langle C \rangle$ and τ are as previously defined and $\tau_{2\mathrm{D}_\mathrm{x}}$ and $\tau_{2\mathrm{D}_\mathrm{y}}$ are the corresponding surface diffusion times in the x-direction and y- direction, respectively.

A regularly observed phenomenon in excitation of molecules is the triplet state. When an electron is excited, it can be elevated into the first excited triplet state which is a forbidden transition. This forbidden state results in the photon not being reemitted during the diffusion through the confocal volume and the electron takes a comparatively long time to relax back to the ground state. Therefore, the fluorescence and the increased intensity cease. The effect of the triplet state must be taken into account in the autocorrelation function.

The triplet state correlation component takes the form

$$G_{\mathrm{triplet}}\,(\tau) = \left[1 + \left(\frac{P_\mathrm{t}}{1 - P_\mathrm{t}}\right) \exp\left(-\frac{\tau}{\tau_\mathrm{t}}\right)\right], \tag{3.43}$$

where P_t is the fraction of electron excitations on the fluorescent molecule that are promoted to the first triplet state and τ_t is the triplet diffusion time: how long the molecule diffuses for and increases the intensity before being excited to the first triplet state.

The overall autocorrelation function is therefore a product of either the free three-dimensional or two-dimensional surface autocorrelation functions and the triplet autocorrelation function. In a real system, there will be both surface and free diffusion within the sample and a further modification to the autocorrelation function must be applied to account for this. An additional term is required to account for the fraction of molecules detected that have been adsorbed onto the surface and this is denoted as f. A modification that applies to both 2D and 3D diffusion that incorporates f and the triplet state can be created from the combination of the above functions

$$G\,(\tau) = \frac{G_{\mathrm{triplet}}\,(\tau)}{N} \left[\frac{(1-f)}{\sqrt{\left(1 + \frac{\tau}{\tau_{3\mathrm{D}}}\right)\sqrt{\left(1 + \frac{\tau}{\tau_{3\mathrm{D}}\Gamma^2}\right)}}} + \frac{f}{\sqrt{\left(1 + \frac{\tau}{\tau_{2\mathrm{D}_\mathrm{x}}}\right)\left(1 + \frac{\tau}{\tau_{2\mathrm{D}_\mathrm{y}}}\right)}}\right]. \tag{3.44}$$

A common practice with the autocorrelation function is to normalise it (equation 3.33) as follows

$$G\ (t) = 1 + \frac{\langle \delta I\ (t)\ \cdot \delta I\ (t+\tau)\rangle}{\langle I \rangle^2}\ . \tag{3.45}$$

The addition of 1 ensures that $G\ (t) > 0$ for all t. The ideal autocorrelation function takes the form as shown in figure 3.7, this shows th e individual contributions from triplet state, 3D and 2D diffusion.

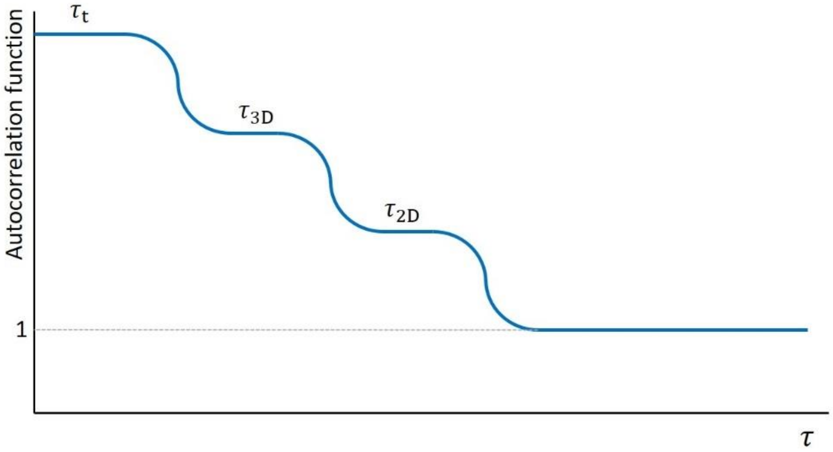

Figure 3.7: Schematic diagram of the combined autocorrelation function including the first triplet state τ_{t}, 3D τ_{3D}, and 2D τ_{2D}, diffusion contributions to the intensity profile. The different contributions will result for specific timescales attributed to each of those contributions. The autocorrelation curve will plateau towards unity once each diffusion component of the fluorescent molecules is removed; the self-similarity will be comparing the intensity of the system without any fluorescence to the background florescence thus no change will be measured.

3.3 Diffusion ordered spectroscopy nuclear magnetic resonance (DOSY NMR)

NMR was first observed in 1945 [110, 111] when it was shown that magnetic nuclei, when under the influence of a magnetic field, are able to absorb radio frequency photons. Different nuclei absorb different energies of photons hence differentiation between constituent species is possible. The timeline that led to DOSY from conventional NMR expands over 40 years, from the first set of self-diffusion coefficients [112], the magnetic field gradient coil being created [113] and an introduction of data processing that allows a 2D plot of frequency against diffusion coefficient to be produced [114].

The principles behind NMR and DOSY NMR will be briefly addressed, considering the underlying physical principles, how data are measured and how properties of the species involved can be extrapolated from those data.

Atoms and molecules have an intrinsic property called spin, the quantum number that describes the magnetic dipole and is a form of angular momentum. Spin has vector properties, possessing both magnitude and a direction. For the ideal case in an NMR experiment, a magnetic field is applied and the spin can either align with the field or against it, the atoms with higher energy will align against it. A source produces radio frequency electromagnetic photons with the corresponding energy of light to align the atoms against the magnetic field and elevate the atoms into the higher energy state. This source is then switched off so the atoms then relax down to their ground state and reemit the absorbed photons creating an intensity signal which is then detected (see figure 3.8). This intensity signal can be used to infer properties such as molecular species and diffusion coefficient.

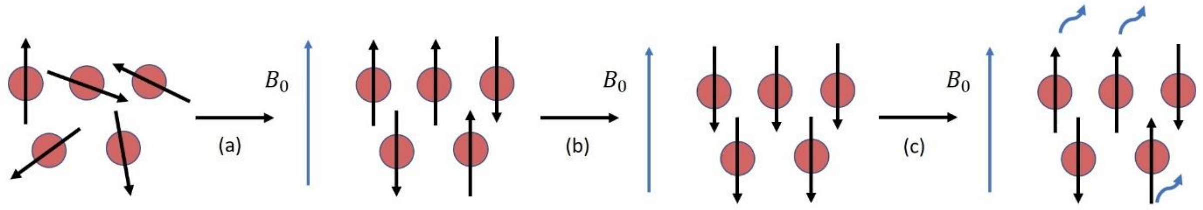

Figure 3.8: Schematic diagram of NMR. (Left to right) A collection of atoms, red circles, that possess a random arrangement of spin, thick black arrows. (a) A magnetic field is applied, blue vertical line, this aligns the atoms spin with lower energy and those with higher energy align anti-parallel to the magnetic field. (b) A radio frequency (RF) source projects photons onto the atoms such that they all now align anti-parallel. (c) Finally, the RF source is switched off, the original lower energy atoms relax to their ground state reemitting the photons, the blue curly arrows.

What data can be extrapolated is linked to the spin property and the magnetic field applied. Firstly, consider the spin of an atom. When an external magnetic field is applied the magnetic moments of the atoms either align parallel or anti-parallel along the axis of the external magnetic field. Those that align with the external magnetic field create a net magnetic field vector. Zeeman splitting takes place so the spin of the atoms takes one of two values with associated energies, the difference between these energies, ΔE, is defined by

$$\Delta E = -\hbar \gamma B_0, \tag{3.46}$$

where $\hbar$ is Planck's constant divided by 2π, γ is the gyromagnetic ratio i.e. the ratio of the magnetic moment to angular momentum of the sample and B_0 is magnetic field strength. When a magnetic field is applied the atoms will precess about their axes with a frequency, f, equal to the Larmor frequency

$$f = -\frac{\gamma B_0}{2\pi}. \tag{3.47}$$

Once the RF pulse is removed, the magnetisation will begin to relax, this changing magnetic field will induce a current in the same RF coil. The measured current, the signal, is shown as a decaying oscillatory wave as the precession of the atoms begins to slow and the circle traced out reduces.

The energy value of the RF pulse is dependent on the effective magnetic field of the nucleus. The surrounding electrons and neighbouring atoms have their own magnetic fields which produce magnetic shielding opposing the applied magnetic field. This opposition alters the frequency required to flip the alignment and can be used to determine the nature of the surrounding species. However, the magnetic shielding must be accounted for in data acquirement and provides a more understandable plot in terms of ppm instead of a frequency. To account for th e magnetic shielding, a dimensionless term is defined, the chemical shift, δ

$$\delta = \frac{f - f_{\mathrm{ref}}}{f_{\mathrm{ref}}} \,, \tag{3.48}$$

where f_{ref} is the reference frequency. The reference material's chemical shift is defined as zero. Species with higher electron affinities will result in smaller chemical shifts as the magnetic shielding will be lower and vice-versa. An example of a standard is D_2O.

The common nuclei used in NMR are ^1H, ^2H and ^{13}C as they are abundant in the samples used thus produce a high attenuation of signal.

DOSY uses a series of magnetic field gradient pulses. The molecular species possessing a larger magnetic dipole moment will diffuse to the higher magnetic field magnitude in the field gradient. All spins of a molecule will have the same diffusion coefficient so DOSY NMR correlates the recorded signal with the corresponding diffusion. The pulses have amplitude, g, and width δ.

The Stejskal-Tanner equation [115] is used to fit the data and is defined as follows

$$I = I_0 \exp\left(-D\gamma^2 g^2 \delta^2 \left(\tau_{\mathrm{D}} - \frac{\delta}{3}\right)\right) \cdot \tag{3.46}$$

Here, I is the measured intensity, I_0 is the reference intensity, D is the diffusion coefficient, γ is the gyromagnetic ratio of the observed nucleus, g is the gradient strength and δ is the duration of the gradient (pulses of magnetic field). This equation can be simplified by combining parameters yield

$$I = I_0 \exp(-DQ) \,,$$

where

$$Q = \gamma^2 g^2 \delta^2 \left(\tau_{\mathrm{D}} - \frac{\delta}{3}\right) \cdot$$

CHAPTER 4: RPEG diffusion on thin polymer films

The two-dimensional diffusion of fluorescently tagged poly(ethylene glycol) (PEG) across bare silicon, poly(ethyl methacrylate) (PEMA) and polystyrene (PS), at temperatures including their respective glass transition temperature, is the main focus of this work. The fluorescent tag is rhodamine-B and the total molar mass of the rhodamine-B-PEG (RPEG) is 20 kDa. Using very low concentrations of RPEG, single molecule diffusion can be achieved within the confocal volume of an FCS experiment. To monitor how the 2D diffusion changes across the glass transition range, the individual T_g of the polymer thin films must first be determined via ellipsometry.

4.1 Experimental Method

To produce the polymer thin films:

a. Silicon wafer substrates with (100) orientation (Prolog Semicor, Ukraine) were cut to 1.5 cm^2 sections using a diamond-tipped scribing pen.
b. Cleaning the substrates required rinsing each individual substrate with deionised water (DI water), all DI water used in this work was collected from a Purelab Q-option with ELGA biofilter at 15 MΩ cm.
c. The substrates are then dried with nitrogen and placed into a custom-built plasma oxidiser for 1 hr.
d. The substrates were then placed into a container that contained Hellmanex, a surfactant given to me by one of my colleagues, with boiled DI water, all of which underwent sonificiation for 15 min in a Branson 2510 ultrasonic cleaner. Hellmanex is used in the preparation of thin films in solar cell work [116].
e. The substrates are then sonicated again in boiled DI water for 5 mins and a final sonication for 15 mins using propan-2-ol.
f. After another 1 hr in the plasma oxidiser, the substrates were immediately coated with the polymer, using spin coating [117-119]. A Laurell Technologies Corporation model number WS-400BZ-6NPP-LITE spincoater was used for all spincoating work.

All polymers (PEMA, PS and RPEG), rhodamine-B, Hellmanex and propan-2-ol had been previously purchased prior to this work commencing, only the toluene solvent had been purchased during this work. The 250 kDa PEMA powder was purchased from Scientific Polymer Inc., 225 kDa PS was originally acquired from Polymer Source Inc., the 20 kDa RPEG was purchased from Nanocs Inc and 99.5% (HPLC) rhodamine-B is bought from Sigma Aldrich Inc. The polymers were of polymer grade. The propan-2-ol was purchased from Acros Organics (Thermo Fisher Scientific) and is 99.5% pure. Anhydrous 99.8% toluene was bought from Sigma Aldrich Inc. All purchased items were used as delivered with no modifications.

With reference to earlier work [129], the required spin speeds, for a given molar mass, to produce the desired film thicknesses were known. Each polymer solution had a specific concentration in order to achieve the optimal thicknesses for a given range of spincoating speeds. PEMA and PS were measured out to achieve 5% w/v solutions with toluene as the solvent. Spin speeds of 4000 RPM were used to achieve thicknesses in the range of 200-300 nm. The inconsistency would arise from contaminations in the solutions or substrate cleaning process. To test whether the substrates had been contaminated, a reflection microscope can be used to view the surface.

It has been reported that after spincoating, there remains residual solvent within the films [120]. Therefore, after spincoating, each film was placed in a vacuum oven at a temperature at least 30 K above its literature T_g value to evaporate any residual solvent. The films were kept in the oven for a minimum of 12 hr. Once complete, each film was then placed onto a controlled heat cycle, again to at least 30 K above its literature T_g at 3 K/min increments, to allow the film to thermally expand at a constant rate such that the polymer chains can equilibrate isotropically, an annealing process. The film is then allowed to cool down to room temperature.

A Linkam heating stage (Linkam Scientific Instruments Ltd, Surrey, UK) connected to a TMS94 heat controller (error: ± 0.1 K) were used to control the temperatures of the polymer thin films. For FCS measurements, a custom-built mount for the heating stage was used to secure it in the confocal microscope platform.

4.2 Measuring T_g using ellipsometry

Polymer thin films are of the nanometre order, to probe this scale, sensitive techniques are required. There are a variety of methods to measure parameters of polymer thin films in order to deduce the glass transition temperature. Ellipsometry is a non-invasive technique that measures the thermal expansion of a material as its temperature is varied [122-124]. By measuring the change in polarisation upon reflection in a thin film over a sample-average (see section 3.1) and fitting this data to a model, properties such as thickness can be retrieved. It is with this method that the glass transition of PEMA and PS films are determined.

An alternative method is x-ray reflectometry (XR) [106-108]. This method relies on the reflection of x-rays from a surface and measures the intensity reflected. There will be some transmission and these transmitted x-rays may then be reflected from the substrate and also be detected. There will be a phase difference between the two reflected x-rays that can be used to infer the material's properties such as thickness. Whilst this offers a reliable thickness determination for the nanometre length-scale, due to comparable wavelength, the method is highly susceptible to surface contamination [121].

4.2.1 Expansion coefficients intersection

When a material is subject to heat, it will experience a change in volume that is proportional to the change in temperature. The constant of proportionality of the relationship is the expansion coefficient, α, expressed in the form

$$\Delta t = \alpha \Delta T , \tag{4.1}$$

where Δt and ΔT are the thickness and temper ature change of the material, respectively. The expansion coefficient depends on the material's state such that any change in state will result in a change in expansion coefficient. This can be represented in a gradient change of a temperature-volume or temperature-thickness graph (figure 4.1). For the case of the transition between a liquid and an amorphous state, the point where the two expansion coefficients intersect is defined as T_{g}.

The main drawback to this method is it assumes that the material instantaneously changes from a liquid to a glass or vice-versa at the glass transition temperature. The change is gradual in real systems and surface transitions occur, whereas in this method they are ignored. However, the expansion coefficient intersection allows a rough glass transition temperature to be estimated.

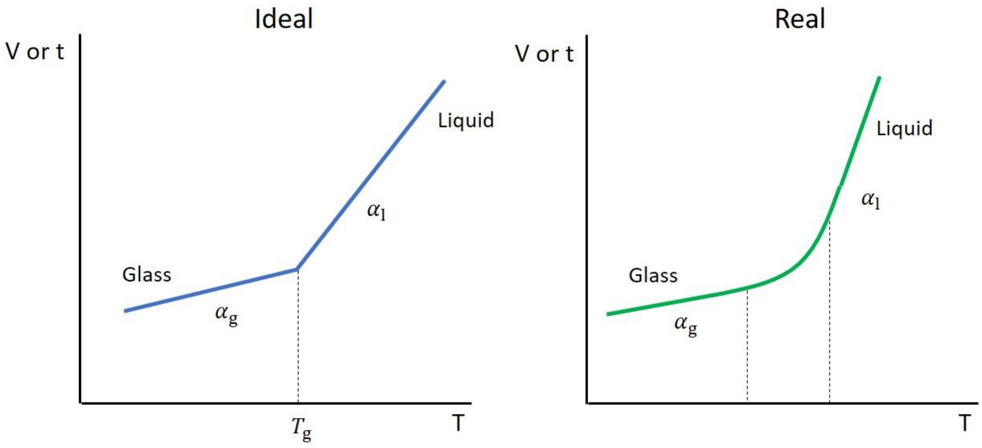

Figure 4.1: Illustration of glass volume (or thickness)-temperature graphs showing glass transitions. The ideal case is an instantaneous transition when the liquid with expansion coefficient α_{l} immediately changes to a glass with expansion coefficient α_{g}. The right-hand side shows the real case where there is a smooth transition, there are still two distinct states however defining a glass transition temperature becomes more difficult.

4.2.2 Numerical differentiation analysis

There are three distinct regions in a thickness-temperature graph of a material undergoing a change from a glass to a liquid or vice-versa: the glass, the liquid and the transition stage. If the gradient of each point on the graph is calculated, the three stages will become distinct sections in a temperature-α graph [83, 125]. For each region, there is a corresponding expansion coefficient, α_{g} and α_{l} for the glass and liquid, respectively, and there will also be a coefficient to describe the transition stage as defined by

$$\alpha(T) = \frac{t\left(T + \frac{\Delta T}{2}\right) - t\left(T - \frac{\Delta T}{2}\right)}{t_0 \Delta T} \tag{4.2}$$

This method can be used to determine the broadening of the glass transition as done with styrene/n-butyl methacylate random copolymers [126] and supported PS films [127].

4.2.3 Results and discussion

Film thickness is measured as a function of temperature and two methods for analysing the data can be applied to determine the value of T_g. The films are heated at 3 K/min with a thickness measurement taken every 3 K after, waiting 3 min to allow the films to equilibrate at that temperature.

To measure the native oxide layer thickness, several clean, bare silicon wafers were used with the ellipsometer at room temperature. The native oxide thickness was measured to be between 1.820 ± 0.011 and 2.900 ± 0.005 nm for different films. To see what effect the different thicknesses had on the polymer film thickness, the different values were used in the model and the only change was to modify the error on the polymer film thickness. Therefore, any value previously measured for the native oxide layer would suffice. In this instance, it was deemed appropriate to use the native oxide layer thickness value that had the lowest error. The software determines the thickness error using a mean squared error equation (MSE). The polymer thin film is heated to 30 K below the respective literature T_g value, from room temperature, at 3 K/min. It is left to equilibrate at the temperature for 3 min. A thickness measurement by the ellipsometer is initiated in the software and recorded. This is repeated for every 3 K increment until the temperature is 30 K above the literature T_g value.

The ellipsometric parameters, as defined by equation 3.14 in section 3.1.2. as a function of the spectroscopic light can be seen in figure 4.2. This raw data is measured using the Alpha-SE ellipsometer by J .A. Woollam Co., Inc. and CompleteEASE v. 5.10 software. The raw data is measured at three different temperatures for a PEMA and PS thin film, including a temperature before, around and after the glass transition temperature. The respective thickness against temperature plots for PEMA and PS are presented in figure 4.3 using the method described in section 4.2.1.

The three different temperatures for PEMA and PS, in figure 4.2, show there is a shift in wavelength as the temperature increases. This is most likely a result of the increasing film thickness causing a larger shift in reflected light. Once the raw data has been measured, it is fitted to a model that is defined in the software. This model is tailored to specific layers and for this work it is a silicon with native oxide and a Cauchy layer on top. The Cauchy layer is used for transparent films and is a method of determining the refractive index of that layer using the ellipsometric parameters. The model also uses the ellipsometric parameters, the amplitude change, Ψ, and phase change, Δ, from the raw data and reinputs these values into the total reflection coefficient as defined in equation 3.25 in section 3.1.3, specifically for elliptical polarisation.

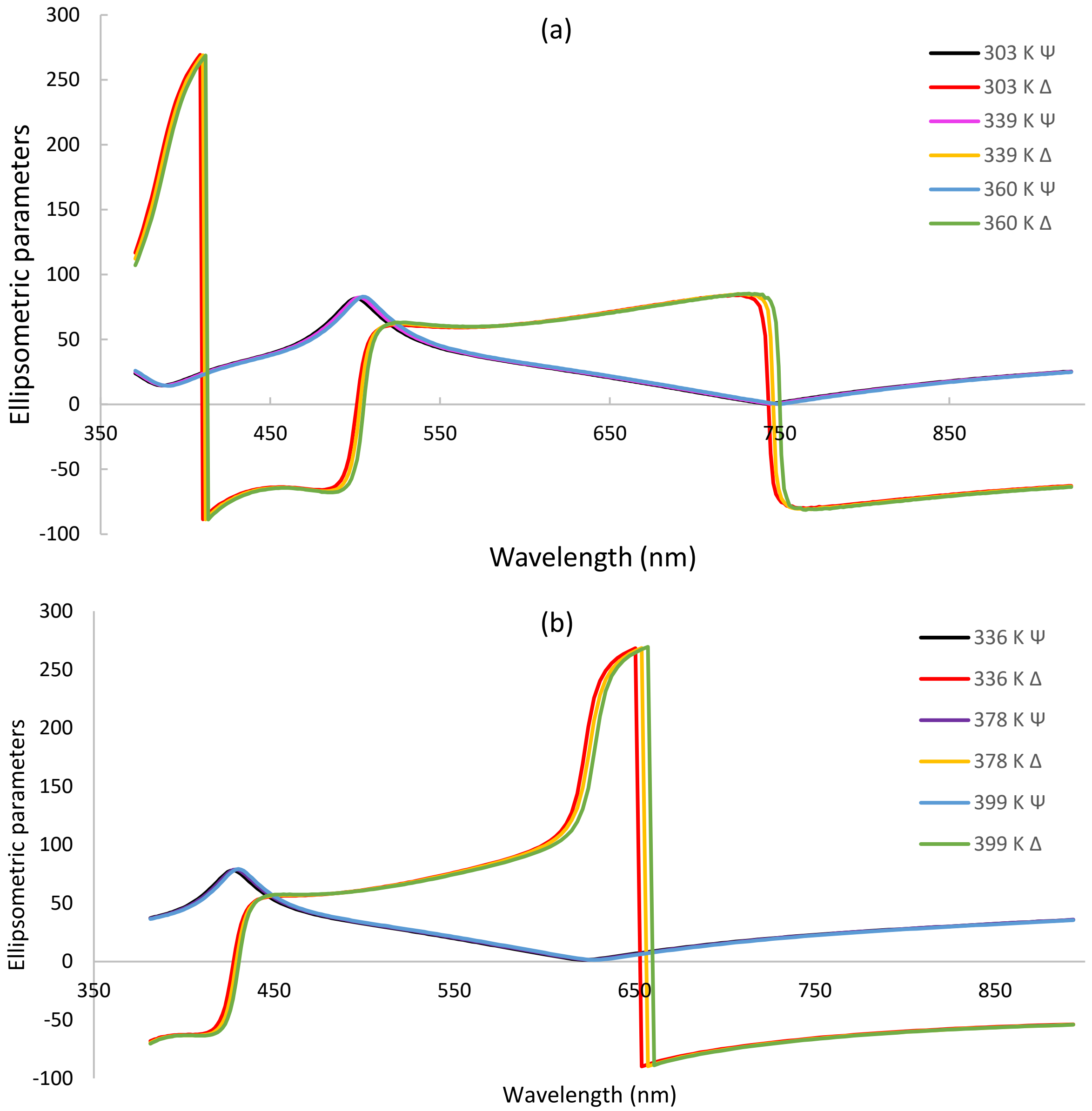

Figure 4.2: Measured ellipsometric parameters (see equation 3.14 in section 3.1.2) as a function of wavelength for PEMA and PS thin films at three different temperatures. Temperatures were chosen to highlight differences between below, at/near and above the glass transition temperature. (a) PEMA ellipsometry data at temperatures 303 K, 339 K and 360 K. (b) PS ellipsometry data at temperatures 336 K, 378 K and 399 K.

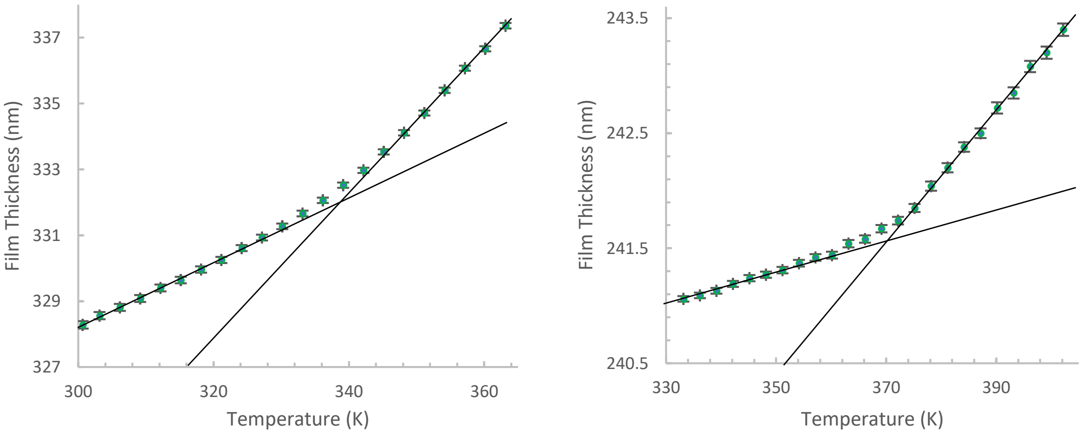

Figure 4.3: Film thickness versus absolute temperature for PEMA (left) and PS (right) using the expansion coefficient method (section 4.2.1) to determine glass transition temperature.

The distinction between the glass and liquid state was chosen as when the change between two thickness points becomes significantly larger than the previous iteration. This does open a degree of discrepancy between where the cut-off point between the two states is but the differences won't be significantly different. The expansion coefficient intersection method determines the measured of PEMA T_g as 335 $\pm$ 7 K and for PS as 371 $\pm$ 8 K. Compared with literature values, the PEMA T_g value has been quoted as 338 K [101] and 339 K [128] which is within good agreement. For PS, the literature T_g values have are between 370-372 K for films of order $10^2\ \mathrm{nm}$ and of a similar molar mass, 120 kDa [10]. The drawback of this method is it determines a single glass transition temperature, this implies there is an instantaneous transition from glass to liquid or vice-versa in the thin film which could explain the large error values. Future work could apply a computer model to the distribution of T_g such that a surface T_g can be defined.

4.3 RPEG diffusion

The reduced T_g in nanoconfined polymer thin films has been rationalised by the presence of a mobile surface layer, with enhanced segmental dynamics (see section 2.3.4). An ideal way to both test this theory and develop an understanding of the mechanisms that cause this layer is to monitor the diffusion of a substance on a polymer thin film as it goes through a glass transition.

To provide context to this work, the two-dimensional diffusion coefficients of 20 kDa fluorescein isothiocyanate tagged PEG (FPEG) on thin polymer films as a function of temperature have been carried out, previously, and the results can be seen in figure 4.4 [129]. The polymer thin films used were poly(methyl methacrylate), poly(ethyl methacrylate), poly(propyl methacrylate) and poly(butyl methacrylate). These specific films were chosen since they have almost identical chemical structure, with each successive polymer having an additional methyl group, and the glass transition temperatures are different. If a similar result for the 2D diffusion coefficients were found then it could be suggested that this is related to the glass transition. It was found that as the thin film reaches its glass transition temperature, the diffusion coefficient of FPEG increases dramatically (e.g. 7× the base value for PEMA) and the diffusion coefficient values would return to a base level. However, the values for the diffusion coefficients were too high and a reason for this was sought. Furthermore, to develop a theory to explain why the diffusion peaks occur, PS is known to be immiscible with PEG [131] and PEMA and PEG are miscible [132, 133], therefore, there should be contrast in the 2D diffusion coefficient trend. By changing the fluorescent molecule this changes the excitation wavelength required.

In this work, FCS is used to measure both 3D and 2D diffusion of RPEG on a bare silicon substrate and a PEMA thin film and DOSY NMR is used to measure only the 3D diffusion coefficient of RPEG. The PEG polymer is fluorescently tagged with rhodamine-B dye, the RPEG molar mass is 20 kDa. A $1\times10^{-9}\ \mathrm{M/L}$ concentration solution was prepared with RPEG dissolved in DI water. An AxioVert inverted confocal microscope with a Zeiss ConfoCor2 FCS module and Zeiss LSM 510 Meta v. 3.2 software were used for the initial diffusion measurements. The objective was a Zeiss C-Apochromat 40x magnification with a numerical aperture equal to 1.2 and a water immersion medium.

To fluoresce a rhodamine-B molecule, a HeNe laser at 543 nm excitation wavelength is used and the beam path is shown in figure 4.4. The laser is switched on an hour before measurements to allow the laser to equilibrate. To calibrate the equipment, the pinhole is aligned with the maximum intensity and count rate using pure rhodamine-B dye:

1. A droplet of DI water, 50 μL, is placed onto the microscope objective and a 96 well, containing a solution of rhodamine-B and DI water, is placed onto a holder and fixed into a stage holder.
2. The microscope objective is then gradually raised and using a camera aligned with the focal point of the lens, the reflected light can be visualised in the confocal software.
3. Once the light has been focussed it implies the surface has been found, in this work that would be the bottom of the 96 well.
4. An intentional increase in height of 200 μm with the microscope objective ensures the light is focussed in the solution, suppressing boundary and surface effects.
5. Refinement of the coarse alignment is then conducted by the LSM 510 Meta software in the ‘Configure’ and ‘Pinhole alignment’ settings until maximum count rate is identified.

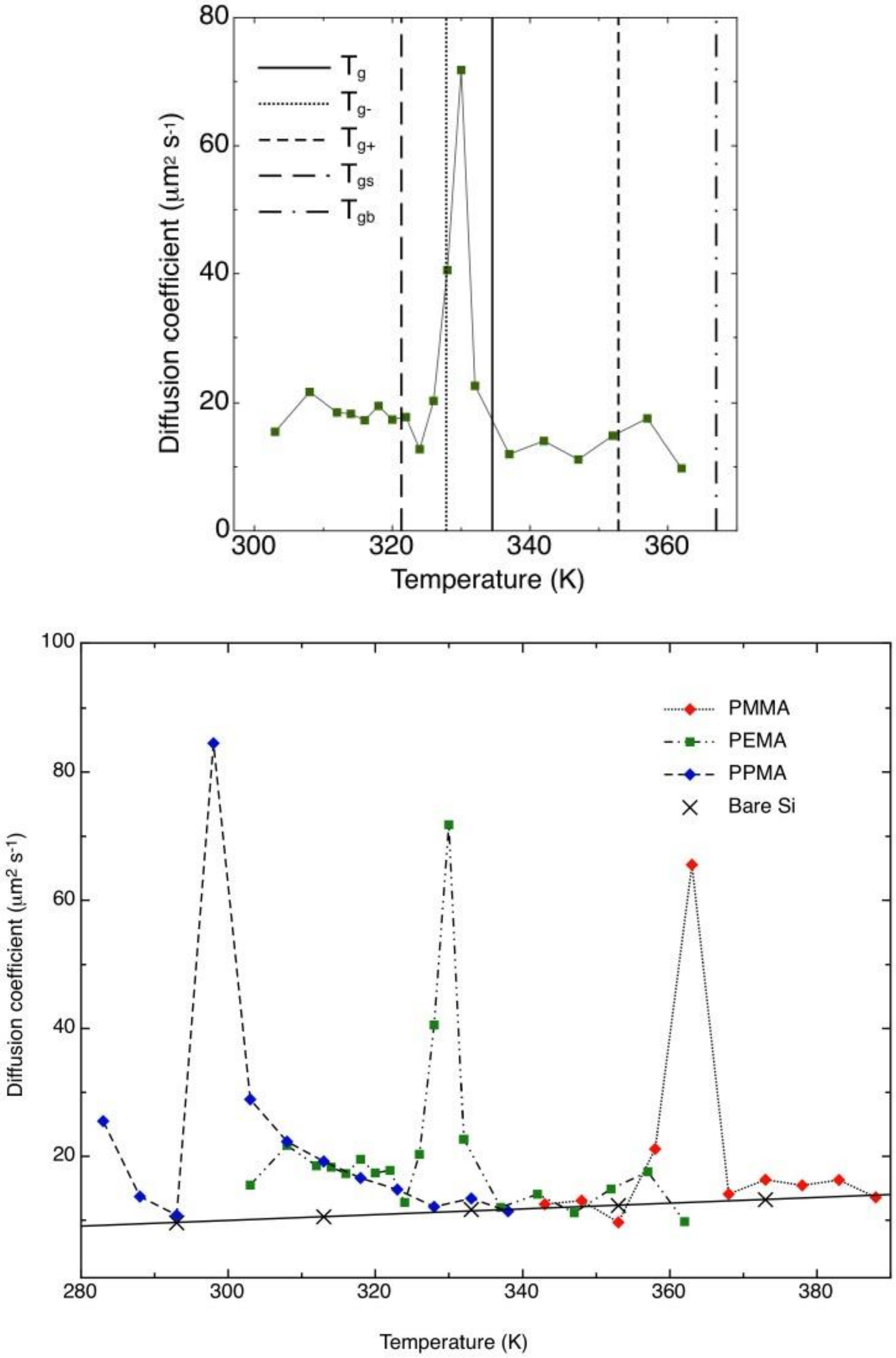

Figure 4.5: 2D diffusion coefficients of FPEG diffusing across a bare silicon surface and PMMA, PEMA and poly(propyl methacrylate) thin films used with permission from reference [129].

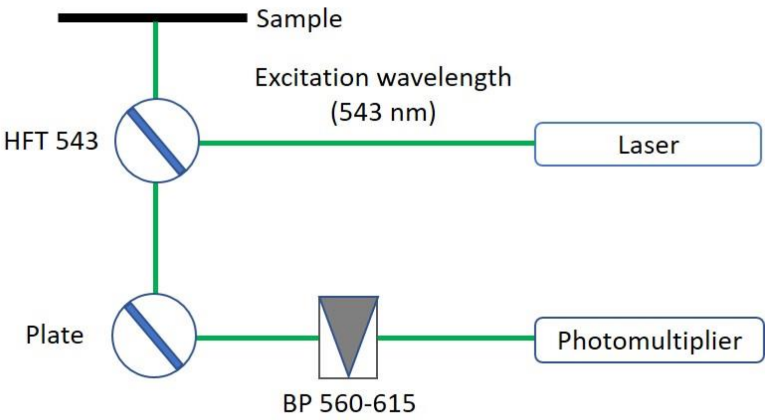

Figure 4.4: Schematic diagram of the beam path used in the FCS measurements, created using the confocal software. The laser (green line) is produced with a wavelength equal to 543 nm. The light passes through a main dichroic beam splitter (HFT 543) and is incident on the sample. The sample then fluoresces and reemits Stoke shifted light at a range of wavelengths. The band pass filter (grey triangle) allows wavelength values between 560-615 nm to reach the photomultiplier.

Using another well in the 96 plate well, steps 1-4 take place with RPEG instead of Rhodamine-B. The analysis procedure is set up in the LSM 510 Meta software to take long measurement times and a number of repeats (60 s, 10 repeats in this work). This ensures that any noise is averaged out. Once the experiment has finished running, the raw data is exported as a text file to a designated save area.

Surface diffusion measurements were conducted in a similar fashion:

i. Beginning with a clean objective and empty stage holder, a small amount, $50\ \mu L$, of the RPEG-DI water solution is applied to the microscope objective as an immersion medium.
ii. The polymer thin film is then placed onto the custom heating stage and fitted onto the stage holder.
iii. The microscope objective is raised to the point where the reflected light is focussed using the confocal software which indicates the surface of the polymer thin film has been found.
iv. Using the Linkam stage, the temperature is increased by different increments with a measurement of the intensity variation taken at each increment as shown in figure 4.6 (b) and (c), each data point corresponds to a temperature increment. The variation ensures that more measurements are taken around where the glass transition temperature is expected. This ascertains a deeper profile of the effect on diffusion coefficient.
v. At each temperature increment, the same 60 s measurement time and 10 repeats are conducted with the raw data exported to a text file.

Each raw data for the autocorrelation curves (figure 4.6 (a)) for each temperature is fitted to equation 3.44, in section 3.2.4 (repeated below), using pro Fit (version 7.0.9, QuantumSoft) fitting software.

$$G\,(\tau) = \frac{G_{\text{triplet}}\,(\tau)}{N}\left[\frac{(1-f)}{\sqrt{\left(1+\frac{\tau}{\tau_{3\text{D}}}\right)\sqrt{\left(1+\frac{\tau}{\tau_{3\text{D}}\Gamma^2}\right)}}}+\frac{f}{\sqrt{\left(1+\frac{\tau}{\tau_{2\text{D}_\text{x}}}\right)\left(1+\frac{\tau}{\tau_{2\text{D}_\text{y}}}\right)}}\right].$$

The data acquired from the 3D experimental setup is used first. The f value is set to zero since it is assumed there is no surface diffusion in the 3D measurements, hence the fraction of adsorbed molecules must be zero. A simple curve fit with Monte Carlo algorithm is used. This acquires values for the triplet state autocorrelation function, the Γ parameter and for 3D diffusion time, $\tau_{3\text{D}}$. The latter can be substituted into equation 2.5 in section 2.1.1, repeated here

$$\tau_{\text{D}} = \frac{x^2}{4D},$$

the value of x is determined by a series of highly precise control experiments used in conjecture with Zeiss when the equipment is first delivered, for this particular equipment, the value is 0.3 μm. Rearranging this τ_{D} equation, the 3D diffusion coefficient can be found. For the 2D data, the fitted 3D values are used with a margin of error arbitrarily defined as $\pm 10\%$ the fitted values. The fraction of adsorbed molecules, f, is no longer fixed. This will produce an overall $\tau_{2\text{D}}$ value, the diffusion time is substituted into the above equation and a 2D diffusion coefficient can be established.

In this work, PEMA was initially used to ensure that the method worked since the glass transition temperature of PEMA is between the freezing and boiling points of water, unlike PS. The RPEG is diluted in water and so the temperature limits are constricted by the boiling and melting point of the water. The results for the 2D diffusion coefficients of RPEG on a PEMA thin film can be seen in figure 4.5 and the corresponding T_{g} is marked. There are two broad peaks, with the greatest increase, exhibiting a $4.5\times$ change in 2D diffusion coefficient, being around the glass transition temperature. The peaks suggest a coupling between the RPEG and surface layer of unknown origin that enhances surface diffusion, however, it is not conclusive and further work is required.

The measured 3D diffusion coefficient of the RPEG was 4800 $\mu\text{m}^2\text{s}^{-1}$, compared to the literature [130] for 20 kDa PEG, the 3D diffusion coefficient was found to be about 100 $\mu\text{m}^2\text{s}^{-1}$ which is 48× smaller than the value produced in this work. Furthermore, the fraction of adsorbed RPEG chains, according to the fitting software, is also shown in figure 4.6. It is interesting to see how the peaks almost line up exactly with the diffusion coefficient peaks. However, it is noted that the range of values of adsorbed chain fraction is $1.31\times 10^{-5} \leq f \leq 7.30\times 10^{-3}$. This is a very low percentage of adsorbed chains, suggesting most of the polymer chains in the confocal volume did not adsorb to the surface and remained in the bulk solution. Another interesting observation is that the larger fraction of adsorbed chains aligns with the smaller of the two peaks and not with the larger peak where the glass transition temperature has been defined.

Comparing the results of figures 4.5 and 4.6 show similar patterns. Both exhibit a peak in surface diffusion near the glass transition temperature, defined by the intersection of expansion coefficients, of the PEMA thin film. The glass transition temperature proceeds a peak in both experiments. Since the smaller peak occurs before the glass transition temperature similar to the single peak in the previous work [129], this would suggest that the smaller peak is RPEG. There is a possible explanation for the two 2D diffusion coefficient peaks in figure 4.6 (b). One peak could correspond to RPEG and the other to dissociated rhodamine-B dye. To verify this dissociated theory, the 3D diffusion coefficient of pure rhodamine-B was measured yielding 5800 $\mathrm{\mu m^2 s^{-1}}$, this is of the same order of magnitude as the results found previously. This does suggest that the measured diffusion coefficients correspond to the rhodamine-B dye. Values from the literature for the 3D diffusion coefficient of rhodamine-B, measured using FCS, yields a value of 420 $\mathrm{\mu m^2 s^{-1}}$ [138]. There is a consistent factor of ten difference between literature 3D diffusion coefficient values and those found in this work.

A potential solution to this issue would be to place the RPEG and DI water solution into a float-a-lyzer G2 dialysis kit (Spectrum Inc.) to, in theory, filter out the dissociated dye leaving behind RPEG, only. Afterwards, further FCS measurements could not reproduce the 2D diffusion coefficient as a function of temperature graph found in figure 4.6 (b). However, the 3D diffusion coefficient of the dialysised RPEG remained at the same order of magnitude.

To test whether the equipment was at fault, dextran that is fluorescently tagged with FITC (FITC-dextran) was purchased from Sigma-Aldrich Ltd, with a molar mass of 20 kDa, within the duration of the work. If the FITC-dextran 3D diffusion coefficient, as measured by the same FCS equipment used for RPEG, is as expected when compared to the literature, this would suggest that the equipment is not at fault for the data in figure 4.6. The 2D diffusion coefficients for FITC-dextran, as a function of temperature, on bare silicon were also measured and can be seen in figure 4.7.

The FITC-dextran 3D diffusion coefficient value at 295 K was measured as 1800 $\mathrm{\mu m^2 s^{-1}}$ and at 363 K it was 860 $\mathrm{\mu m^2 s^{-1}}$. Comparing the 3D values in this work with the literature [134], for 4 kDa the 3D diffusion coefficient is found to be 140 $\mathrm{\mu m^2 s^{-1}}$ and for 40 kDa it is 45 $\mathrm{\mu m^2 s^{-1}}$. It is reasonable, therefore, to expect that for 20 kDa the diffusion coefficient would be between these two values. The results in this work are between 10 and 100× higher than in the literature for the two temperatures measured. Since the results produced for both a new fluorescently tagged polymer, FITC-dextran, and an older polymer, RPEG, have yielded similar results, this indicates that the FCS equipment is one of the possible reasons as to why the 3D diffusion coefficients are so consistently high and of the same order of magnitude.

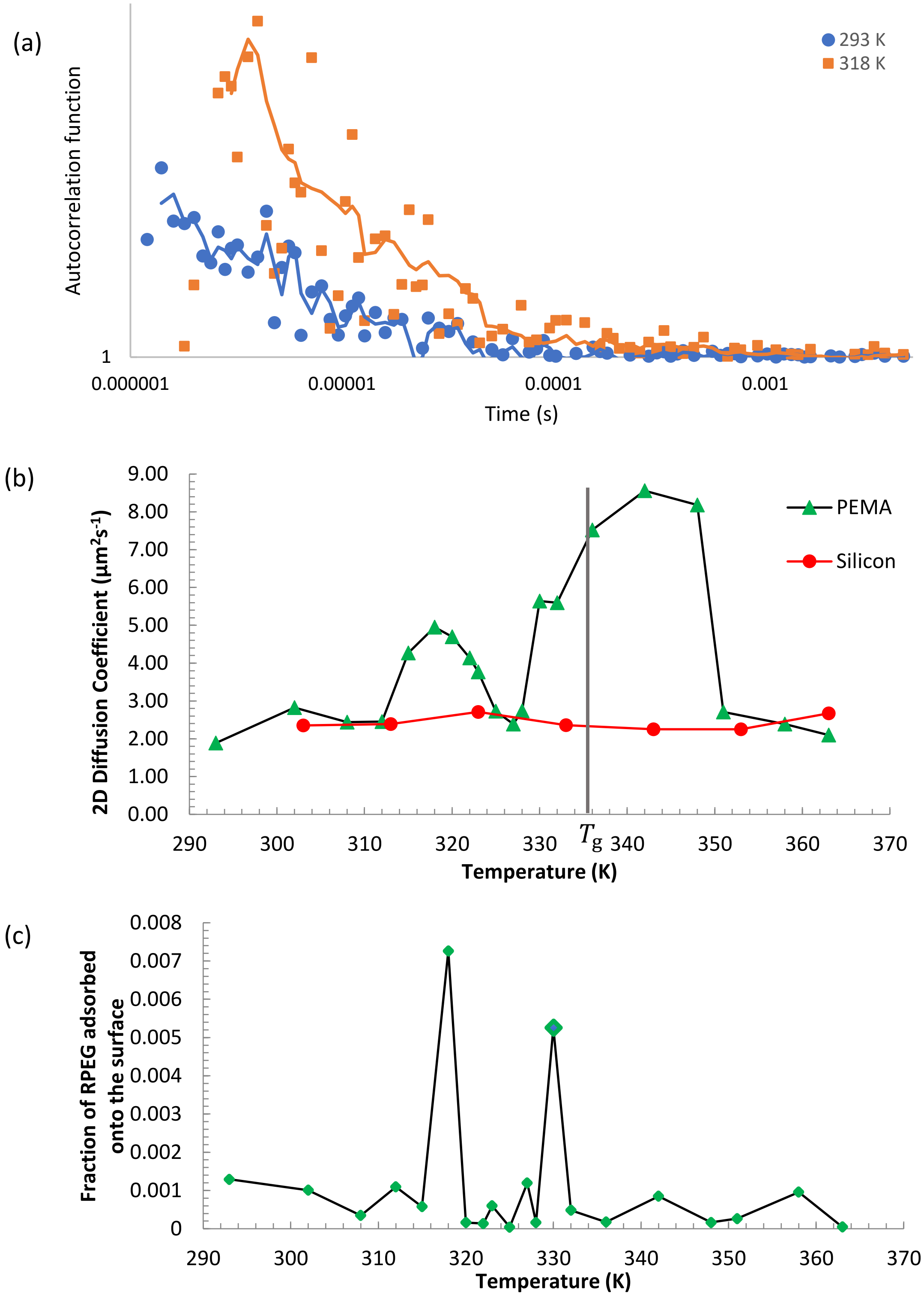

Figure 4.6: (a) Autocorrelation functions, for two different temperatures, against time for a PEMA thin film. The raw data is acquired from the FCS software. (b) Two-dimensional diffusion coefficient curve as a function of temperature for a PEMA thin film (green triangles). The corresponding PEMA glass transition temperature, calculated in section 4.2.3, is marked by a black line and labelled by T_g. The autocorrelation function in (a) corresponds to the same PEMA film. The RPEG 2D diffusion coefficients on a bare silicon surface are shown also (red line and circles). (c) Fraction of RPEG adsorbed onto the surface as a function of temperature, as determined by the fitting software, pro Fit (version 7.0.9, QuantumSoft), using the FCS software data.

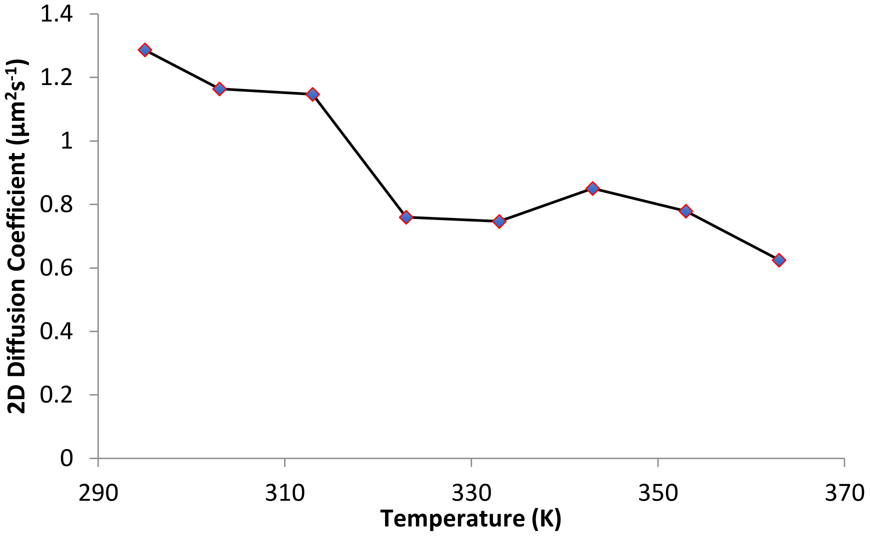

Figure 4.7: 2D diffusion coefficients as a function of temperature for FITC-dextran diffusing on a bare silicon substrate.

With silicon, a linear increase of diffusion coefficients, for a molecule, as a function of temperature is expected as described in section 2.1. However, the 2D diffusion coefficients of FITC-dextran show a downwards trend (figure 4.7). This coincides with the decreasing 3D diffusion coefficient as the temperature is increased from 295 K to 363 K. FITC-dextran diffusion on silicon has not been measured, previously, so if these results are correct, it indicates that there is an unusual effect given rise to a decrease in the diffusion coefficient with increasing temperature.

It is a consistent result, for both RPEG and FITC-dextran, that the count rate on the confocal software is always different to the values produced by the fitting software, even after testing different fitting parameters. It is most likely, that there is an as yet undefined equipment fault that produces the results shown. This would explain why new FITC-dextran is producing the wrong relationship between diffusion coefficient and temperature and why there are orders of magnitude in difference for the diffusion coefficients. Furthermore, the fitting software provides a reduced chi-squared analysis of the data to the model to test the quality of the fit. In all cases, the reduced chi-squared was below 1 which is an indication of the poor results.

To test if the RPEG has degraded, DOSY NMR, using a Bruker Avance III 400, was employed to measure the 3D diffusion coefficient. If it is found that the RPEG has a diffusion coefficient of similar value to the literature, then there is a fault with the FCS equipment alone. If similar 3D diffusion coefficient values were found as has been found in this work so far, then it can be suggested that both the FCS equipment and RPEG have faults. A 100 nM concentration of RPEG was provided for the sample. A capillary tube was placed inside the solution holder, with $\mathrm{D_2O}$ acting as a reference, to avoid any potential mixing between the water and $\mathrm{D_2O}$ that could weaken the signal attenuation. The 100 nM concentration was the highest available concentration due to the dialysis of RPEG restricting the available amount. Using equation 3.46 from section 3.3:

$$I = I_0 \exp\left(-D\gamma^2 g^2 \delta^2 \left(\tau_{\mathrm{D}} - \frac{\delta}{3}\right)\right)$$

the values for I_0, γ and δ are controlled variables and are adjusted to achieve the highest signal attenuation. The raw data is an exponential decay of intensity produced from the recorded signal from the relaxing protons. This data is then fitted to the above intensity equation to extract the diffusion coefficients of the species. The software used is Milicent v. 3.1 and this applies a Monte Carlo algorithm to fit the data and produce the relevant errors. The DOSY NMR results are seen in figure 4.8.

When fitting the raw data to the equation 3.46 in section 3.3, the diffusion coefficient yields $D_{\mathrm{3D}} = (5.7 \pm 0.2)\times 10^3\ \mu\mathrm{m}^2\mathrm{s}^{-1}$. This result is of the same order of magnitude as the RPEG FCS results. Therefore, two values from two different techniques have both found a similar result. A possible explanation could be that only pure dye remains after fully dissociating from the PEG and that is why there is such a low fraction of adsorbed molecules in the RPEG FCS results. In both cases, the RPEG 3D diffusion coefficient is 10 times larger than in the literature. This consistency suggests that, not only is the FCS at fault, but the RPEG is as well. Due to limitations of timing, new RPEG was unable to be purchased. A future test to possibly solve this issue would be to acquire new RPEG or FPEG to repeat the same measurements. The FCS requires a thorough servicing and testing to ensure that the results produced are as expected.

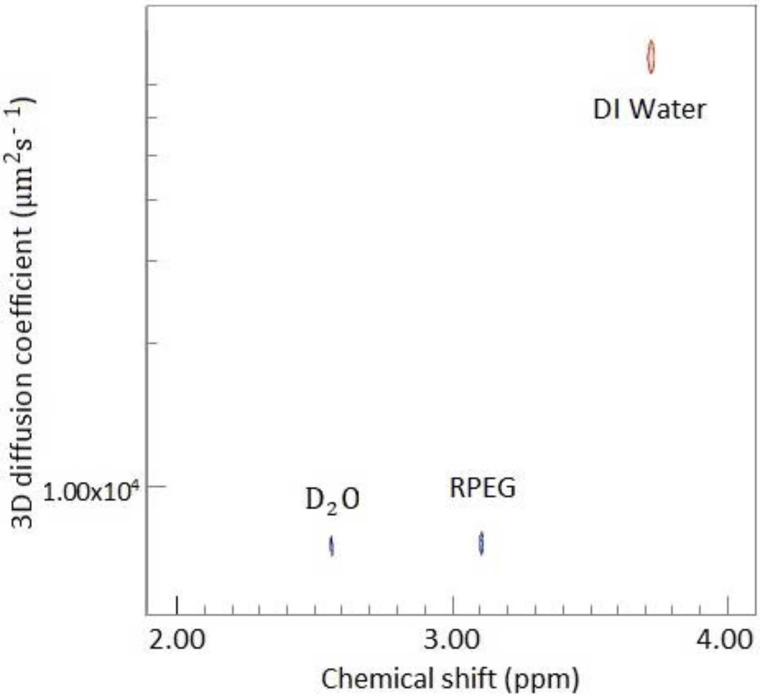

Figure 4.8: The 3D diffusion coefficients measured by DOSY NMR. The diffusion coefficient results for $\mathrm{D_2O}$, RPEG and water are on the left, middle and right respectively.

One final test was to use another piece of FCS equipment. The University of Manchester Systems Microscopy Centre had the Zeiss LSM 780 with ConfoCor 3 and Zeiss ZEN v 2.3 software. The same objective was used in this work. The 3D diffusion measurements of RPEG and pure rhodamine-B dye were found used the same procedure as in Sheffield, the software exports the same raw autocorrelation function data that is then fitted to equation 3.44. After the same methodology used previously, the 3D diffusion coefficients for pure rhodamine-B dye and RPEG were calculated to be 643.61 $\mu\mathrm{m}^2\mathrm{s}^{-1}$ and 631.54 $\mu\mathrm{m}^2\mathrm{s}^{-1}$, respectively. Comparing the two 3D diffusion results, it is quite evident that the RPEG and rhodamine-B have almost identical diffusion coefficients. This is the strongest evidence yet to support the hypothesis that the RPEG has degraded and only pure dye remains. The discrepancy between the two values may be a result of experimental error from contaminations in the solutions or as a result of some PEG remaining associated with the dye causing the slower diffusion. However, it is clear that brand new RPEG would be needed for future work. The raw data for the autocorrelation curve can be seen in figure 4.9, compared to figure 4.6 (a), the latter has a higher scatter indicating a systematic error with the LSM 510 FCS.

Another test was to measure the 3D diffusion coefficient of FITC-dextran, found to be 148 $\mu\mathrm{m}^2\mathrm{s}^{-1}$. This diffusion coefficient is in far greater agreement with the literature, although slightly above that for a larger molar mass version. Since the measured 3D diffusion coefficient of FITC-dextran was of similar order to the literature value, it is suggested that the FITC-dextran has not degraded and the large diffusion 3D coefficient presented previously were caused by the LSM 510 FCS. This is consistent with the difference in RPEG and rhodamine-B diffusion coefficients. FITC-dextran 2D diffusion measurements were then carried out both bare silicon and a PEMA thin film, the results of which can be found in figure 4.9. There is a linear increase in 2D diffusion coefficient as a function of temperature for the bare silicon surface as expected. For the PEMA thin film, there is a gradual increase in diffusion coefficient until about 5 K below the T_g value determined in section 4.2.3. This trend is very similar and consistent to the contextual work [129] (figure 4.5), the diffusion peaks for the separate PEMA thin films (figure 4.5 & figure 4.9) are coherent even for different fluorescent molecules. The diffusion behaviour seems to couple with the glass transition. There appears to be enhanced mobility at a consistent temperature value below the glass transition temperature measured via ellipsometry. The exact reasoning for this is unclear and further work is required, using different FCS equipment or serviced LSM 510 FCS and brand new fluorescently tagged PEG.

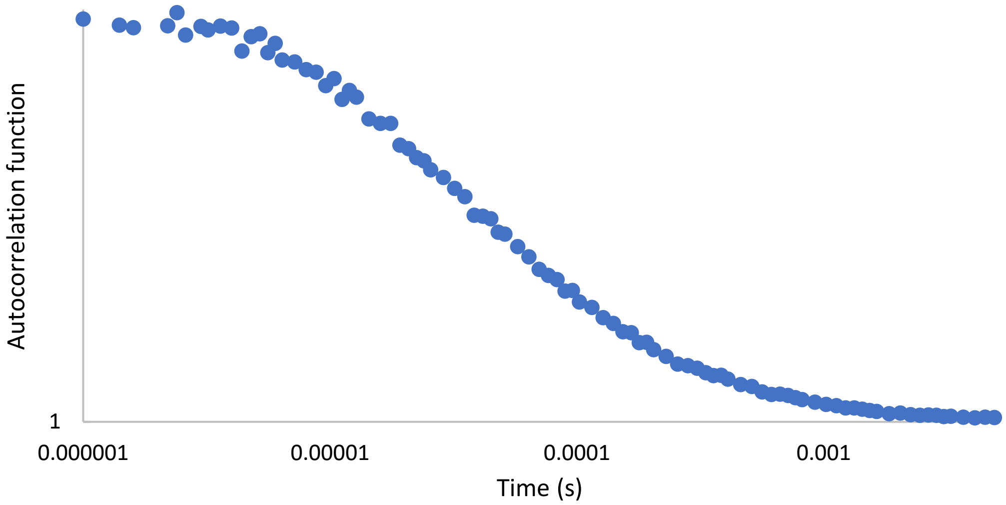

Figure 4.9: Autocorrelation curve showing raw data of a 20 kDa RPEG 3D measurement as measured at the University of Manchester.

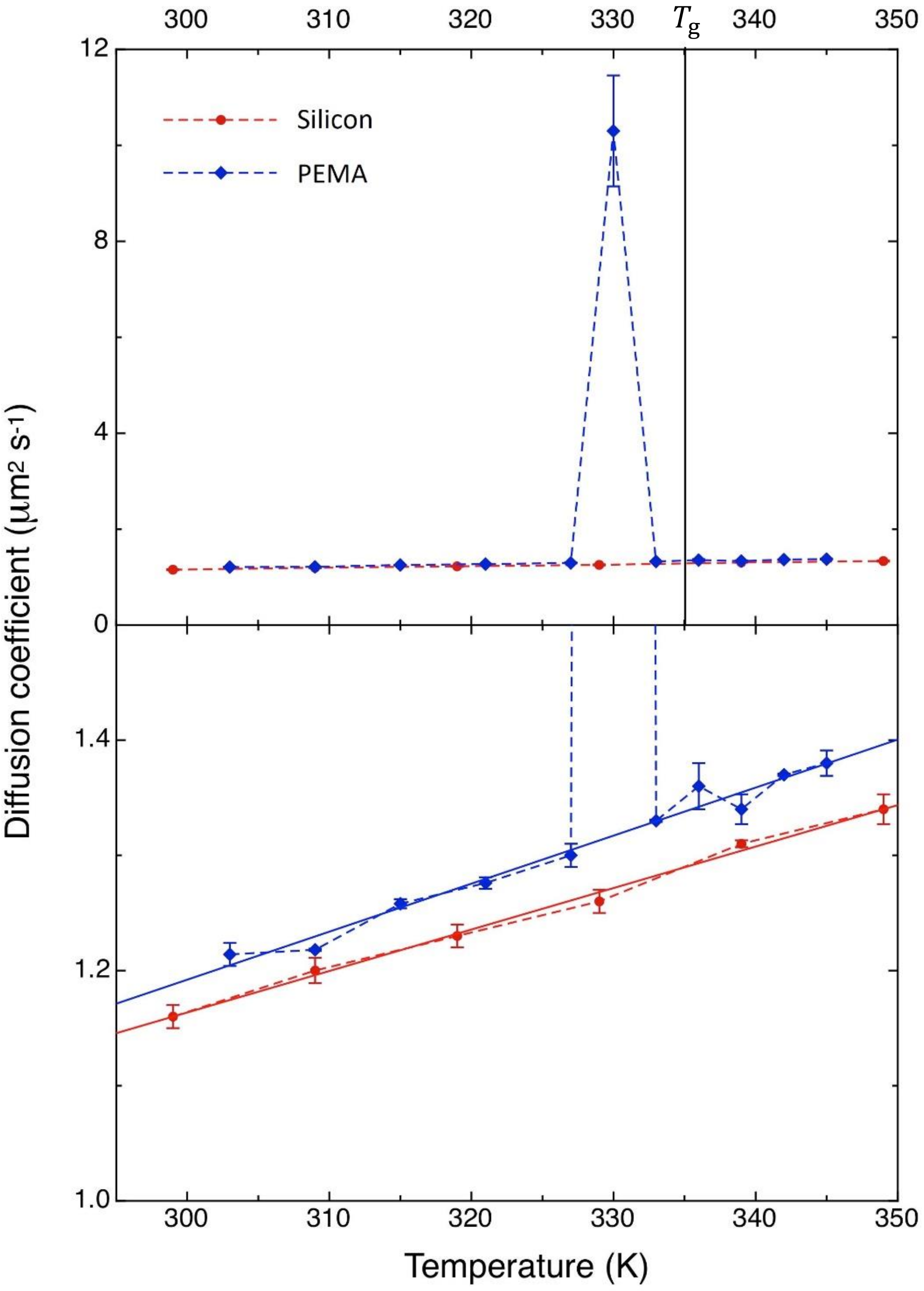

Figure 4.10: The 2D diffusion coefficients, as a function of temperature, for FITC-dextran on silicon (red) and a PEMA thin film (blue). The corresponding PEMA T_g, as determined in 4.2.3, is labelled and denoted by a black line.

CHAPTER 5: Conclusions

Over the past few decades, our understanding of the glass transition of thin polymer films has advanced forward. It is now well known that polymers exhibit deviations from the bulk properties when confined to the nanometre scale. A brief review of what properties are affected upon confinement, the methods to understand the process of vitrification and the evidence that suggests the existence of a distribution of glass transition temperatures throughout a thin film has been conducted in this thesis.

The main aim of this research was to develop the understanding of the mobile surface layer that arises upon confinement in polymer thin films. The method to do this was to monitor how the diffusion of a fluorescently tagged molecule changes as the polymer substrate undergoes a glass transition. This should give key insight into the dynamics of the surface layer as it has a direct influence on the diffusion of the molecule. In order to understand the results, a discussion on the theories of diffusion and polymer adsorption had to be addressed.

Firstly, by using ellipsometry data the glass transition temperature of a PEMA and a PS thin film have been measured. The two glass transition temperatures were in good agreement with the literature values for the respective films. Rhodamine-B-PEG surface diffusion has been observed with fluorescence correlation spectroscopy on a poly(ethyl methacrylate) thin film and on bare silicon across a specific temperature range. There was a heightened surface diffusion of RPEG on PEMA as the glass transition temperature is approached. The 2D diffusion coefficient values were much lower than in the previous work [129] as was aimed for. 3D diffusion coefficients were measured for RPEG using FCS and DOSY NMR and for FITC-dextran using FCS. There was a decreasing surface diffusion coefficient as temperature increased for FITC-dextran on silicon that provides interesting possibilities for future research.

However, there are opportunities for future work. The results suggested that the FCS equipment was not working to standard by yielding consistent values of 3D diffusion coefficients that were orders of magnitude higher than in the literature for two different fluorescently tagged molecules, RPEG and FITC-dextran. Measurements of the pure dye, rhodamine-B, add to the evidence of faulty equipment as, it too, had a 3D diffusion coefficient of similar order of magnitude to the aforementioned molecules. By testing the RPEG with another experimental method, DOSY NMR, it was found that the 3D diffusion coefficient was of a similar value to those found by FCS. This adds further suspicion that the FCS equipment was not at fault solely. Instead, it seems as though both the FCS and the RPEG are the problems. In order to rectify this, new RPEG or FPEG should be purchased and tested on the FCS after thorough fixing of the equipment.

New equipment was used at The University of Manchester. The 3D diffusion coefficients of RPEG and pure rhodamine-B were found to be similar order, this increases the evidence that RPEG had in fact degraded. FITC-dextran’s 3D diffusion coefficient was also measured and found to be consistent with the literature. This supports the theory that the LSM 510 equipment used previously is in need of servicing. The 2D diffusion coefficients for

FITC-dextran on silicon and a PEMA thin film were found to exhibit the behaviour shown in the previous work, that this research is based on [129], at lower values. There is indeed a peak in surface diffusion coefficient for a PEMA thin film at a temperature of 5 K below the glass transition temperature measured in this work. It is clear the LSM 510 FCS and RPEG require replacing.

A continuation of this work would require the LSM 510 FCS to be serviced or continue using the equipment at Manchester with brand new fluorescently tagged PEG. Different film thicknesses could be tested to examine the difference in diffusion peak height. As discussed earlier [10], there is a thickness dependence of glass transition temperature, if there is a more mobile surface layer, this effect should be amplified with thinner films and should result in different diffusion peak heights with the PEG surface diffusion. Repeating the same RPEG surface diffusion on PEMA and a PS thin film will add confidence to this and previous work [129].

References

[1] J. V. Cartmell and W. R. Sturtevant. US Patent **5** 106,629; 1992.

[2] D. R. Holm, S. A. Burton, R. A. Asmus and R. L. Jacobson. US Patent 2011/0166492 A1; 2011

[3] V. K. Vendra, L. Wu and S. Krishnan. *Polymer Thin Films for Biomedical Applications. Nanotechnologies for the Life Sciences*. 2011.

[4] L. Xiao, Y. Xinhong and H. Yanchun. Polymer thin films for antireflection coatings. *J. Mater. Chem. C*. **1** 2266-2285, 2013.

[5] D. B. Hall, R. D. Miller and J. M. Torkelson. Molecular probe techniques for studying diffusion and relaxation in thin and ultrathin polymer films. *J. Polym. Sci. B Polym. Phys.*, **35** 2795-2802, 1997.

[6] J. L. Keddie, R. A. L. Jones, and R. A. Cory. Size-Dependent Depression of the Glass Transition Temperature in Polymer Films. *Europhys. Lett.*, **27** 59 64, 1994.

[7] J. A. Forrest, K. Dalnoki Veress, and J. R. Dutcher. Interface and chain confinement effects on the glass transition temperature of thin polymer films. *Phys. Rev. E*, **56** 5705-5716, 1997.

[8] K. Dalnoki-Veress, J. A. Forrest, C. Murray, C. Gigault, and J. R. Dutcher. Molecular weight dependence of reductions in the glass transition temperature of thin, freely standing polymer films. *Phys. Rev. E*. **63** 031801, 2001.

[9] L. H. Zhang, R. Elupula, S. M. Grayson J.M. and Torkelson. Major impact of cyclic chain topology on the Tg-confinement effect of supported thin films of polystyrene. *Macromolecules*. **49** 257–68, 2016.

[10] J. L. Keddie, R. A. L. Jones R. A. and Cory. Interface and surface effects on the glass-transition temperature in thin polymer-films. *Faraday Discus*. **98** 219–30, 1994.

[11] D. S. Fryer, R. D. Peters, E. J. Kim, J.E. Tomaszewski, J. J. de Pablo, P. F. Nealey. Dependence of the Glass Transition Temperature of Polymer Films on Interfacial Energy and Thickness. *Macromolecules*. **34** 5627–5634, 2001.

[12] J. H. Kim, J. Jang, W. C. Zin. Thickness Dependence of the Glass Transition Temperature in Thin Polymer Films. *Langmuir*. **17** 2703–2710, 2001.

[13] P. G. de Gennes. Glass transitions in thin polymer films. *Eur. Phys. J. E*. **2** 201–205, 2000.

[14] C. J. Ellison and J. M. Torkelson. The distribution of glass-transition temperatures in nanoscopically confined glass formers. *Nat. Mater*. **2** 695–700, 2003.

[15] Z. H. Yang, Y. Fujii, F. K. Lee, C. H. Lam and O. K. C. Tsui. Glass transition dynamics and surface layer mobility in unentangled polystyrene films. *Science*. **328** 1676–9, 2010.

[16] M. Chowdhury, Y. Guo, Y. Wang, W. L. Merling, J. H. Mangalara, D. S. Simmons, R. D. Priestley. Spatially Distributed Rheological Properties in Confined Polymers by Noncontact Shear. *J. Phys. Chem. Lett.* **8** 1229–1234, 2017.

[17] M. Rubinstein and R. H. Colby. *Polymer Physics*. Oxford University Press, Oxford, 2013.

[18] R. A. L. Jones. *Soft Condensed Matter*. Oxford University Press, New York, 2004

[19] S. Napolitano, S. Capponi and B. Vanroy. Glassy dynamics of soft matter under 1D confinement: how irreversible adsorption affects molecular packing, mobility gradients and orientational polarization in thin films. *Eur. Phys. J. E.* **36** 37, 2013.

[20] S. Napolitano, E. Glynos and N. B. Tito. Glass transition of polymers in bulk, confined geometries, and near interfaces. *Rep. Prog. Phys.* **80** 036602, 2017.

[21] Messe Düsseldorf and PlasticsEurope Deutschland Plastics - the Facts 2016. *Plastics Europe*. 2016.

[22] R. Brown. A brief account of microscopical observations made in the months of June, July and August, 1827, on the particles contained in the pollen of plants; and on the general existence of active molecules in organic and inorganic bodies. (Not published), 1827.

[23] G. G. Stokes. *Collected Mathematical and Physical Papers*. Cambridge, University Press, Cambridge, 1880.

[24] A. Einstein. On The Movement Of Small Particles Suspended In Stationary Liquids Required By The Molecular-Kinetic Theory Of Heat. *Annalen der Physik*. **17** 549-560, 1905.

[25] B. K. Varma, Y. Fujita, M. Takahashi, and T. Nose. Hydrodynamic radius and intrinsic viscosity of polystyrene in the crossover region from theta to good-solvent conditions. *J. Poly. Sci. Poly. Phys. Edu*., **22** 1781-1798, 1984.

[26] R. Zwanzig and A. K. Harrison. Modifications of the Stokes-Einstein formula. *J. Chem. Phys.* **83** 5861-5862, 1985.

[27] G. L. Pollack and J. J. Enyeart. Atomic test of the Stokes-Einstein law. II. Diffusion of Xe through liquid hydrocarbons. *Phys. Rev. A.* **31** 980-984, 1985

[28] J. Liu, D. Cao and L. Zhang. Molecular Dynamics Study on Nanoparticle Diffusion in Polymer Melts: A Test of the Stokes−Einstein Law. *J. Phys. Chem. C.* **112** 6653–6661, 2008.

[29] T.C. Chan, K.Y. Li, H.T. Li. Diffusion of spherical solutes: A fractional molecular-hydrodynamic study of solvent dependence. *Chem. Phys*. **468** 25-36, 2016.

[30] H. R. Schober and H. L. Peng. Heterogeneous diffusion, viscosity, and the Stokes-Einstein relation in binary liquids. *Phys. Rev. E.* **93** 052607, 2016.

[31] P.E. Rouse. A Theory of the Linear Viscoelastic Properties of Dilute Solutions of Coiling Polymers. *J. Chem. Phys.* **21** 1272-1280, 1953.

[32] J. D. Scheiber and H. C. Oettinger. The effects of bead inertia on the Rouse model. *J. Chem. Phys.* **89** 6972-6981, 1988.

[33] J. R. Prakash. Rouse Chains with Excluded Volume Interactions: Linear Viscoelasticity. *Macromolecules*. **34** 3396-3411, 2001.

[34] P. Degond, A. Lozinski, R.G. Owens. Kinetic models for dilute solutions of dumbbells in non-homogeneous flows revisited. *J. Non-Newton. Fluid Mech.* **165** 509–518, 2010.

[35] G. G. Vogiatzis, G. Megariotis, and D. N. Theodorou. Equation of State Based Slip Spring Model for Entangled Polymer Dynamics. *Macromolecules*. **50** 3004–3029, 2017.

[36] V. C. Chappa, D. C. Morse, A. Zippelius, M. Müller. Translationally Invariant Slip-Spring Model for Entangled Polymer Dynamics. *Phys. Rev. Lett*. **109** 148302, 2012.

[37] H. Vandebroek, C. Vanderzande. On the Generalized Langevin Equation for a Rouse Bead in a Nonequilibrium Bath. J. Stat. Phys. **167** 14, 2017.

[38] R. B. Bird, P. J. Dotson, and N. L. Johnson. Polymer solution rheology based on a finitely extensible bead-spring chain model*. J. Non- Newtonian Fluid Mech.* **7** 213-235, 1980.

[39] R. C. Armstrong. Kinetic theory and rheology of dilute solutions of flexible macromolecules. I. Steady state behaviour*. J. Chem. Phys*. **60** 724-728, 1974.

[40] R. C. Armstrong. Kinetic theory and rheology of dilute solutions of flexible macromolecules. II. Linear viscoelasticity*. J. Chem. Phys*. **60** 729-733, 1974.

[41] B. H. Zimm. Dynamics of Polymer Molecules in Dilute Solution: Viscoelasticity, Flow Birefringence and Dielectric Loss*. J. Chem. Phys.* **24** 269-278, 1956.

[42] S. R. Quake. The Zimm Model Applied to Extended single polymers*. J. Chem. Phys.* **101** 4307-4311, 1994.

[43] R. Wenczel and C.-Y. Shew. Extension of the Zimm and Rouse model to a polymer chain confined by a harmonic potential in theta-solvent conditions*. J. Chem. Phys.* **116** 9537-9544, 2002.

[44] S. F. Edwards. The statistical mechanics of polymerized materials*. Proc. Phys. Soc.* **92** 9, 1967.

[45] P. G. de Gennes. Reptation of a polymer chain in the presence of fixed obstacles*. J. Chem. Phys.* **55** 572, 1971.

[46] M. Doi. Explanation for the 3.4 power law of viscosity of polymer liquids on the basis of the tube model*. J. Polym. Sci. Polym. Lett. Ed.* **19** 265, 1981.

[47] E. J. Donth. *The glass transition: relaxation dynamics in liquids and disordered materials*. Springer, Berlin, 2001.

[48] D. J. Wales*. Energy Landscapes: Applications to Clusters, Biomolecules, and Glasses.* (Cambridge: Cambridge University Press), 2004.

[49] G. Adam and J. H. Gibbs. On temperature dependence of cooperative relaxation properties in glass-forming liquids*. J. Chem. Phys.* **43** 139, 1965.

[50] T. R. Kirkpatrick, D. Thirumalai and P. G. Wolynes. Scaling concepts for the dynamics of viscous-liquids near an ideal glassy state*. Phys. Rev. A.* **40** 1045–54, 1989.

[51] V. Lubchenko and P. G. Wolynes. Theory of structural glasses and supercooled liquids. Annu*. Rev. Phys. Chem.* **58** 235–66, 2007.

[52] J. C. Dyre, N. B. Olsen and T. Christensen. Local elastic expansion model for viscous-flow activation energies of glass-forming molecular liquids. *Phys. Rev. B.* **53** 2171–4, 1996.

[53] T. G. Fox and P. J. Flory. 2nd-order transition temperatures and related properties of polystyrene. 1. Influence of molecular weight. *J. Appl. Phys*. **21** 581–91, 1950.

[54] D. Turnbull and M. H. Cohen. Free-volume model of the amorphous phase: glass transition*. J. Chem. Phys.* **34** 120, 1961.

[55] R. P. White and J. E. G. Lipson. Free volume in the melt and how it correlates with experimental glass transition temperatures: results for a large set of polymers. *ACS Macro Lett.* **4** 588–92, 2015.

[56] R. P. White and J. E. G. Lipson. How free volume does influence the dynamics of glass forming liquids. *ACS Macro Lett.* **6** 529–534, 2017.

[57] L. Berthier, G. Biroli, J. P. Bouchaud, L. Cipelletti and W. van Saarloos. *Dynamical Heterogeneities in Glasses, Colloids and Granular Materials.* (Oxford: Oxford University Press), 2011.

[58] L. Berthier. Dynamic heterogeneity in amorphous materials. *Physics*. **4** 42, 2011.

[59] S. C. Glotzer. Spatially heterogeneous dynamics in liquids: insights from simulation. *J. Non-cryst. Solids.* **274** 342–55, 2000.

[60] F. W. Starr, J. F. Douglas and S Sastry. The relationship of dynamical heterogeneity to the Adam–Gibbs and random first-order transition theories of glass formation. *J. Chem. Phys.* **138** 12A541–9, 2013.

[61] G. Tarjus, S. A. Kivelson, Z. Nussinov and P. Viot. The frustration-based approach of supercooled liquids and the glass transition: a review and critical assessment. *J. Phys.:Condens. Matter.* **17** R1143–82, 2005.

[62] R. P. White and J. E. G. Lipson. Thermodynamic treatment of polymer thin-film glasses. *Phys. Rev. E.* **84** 041801, 2011

[63] R. A. L. Jones and R. W. Richards. *Polymers at Surfaces and Interfaces.* (Cambridge University Press: Cambridge, UK), 1999.

[64] S. Peter, H. Meyer and J. Baschnagel. Thickness-dependent reduction of the glass-transition temperature in thin polymer films with a free surface. *J. Polym. Sci. B.* **44** 2951–67, 2006.

[65] J. A. Forrest and K. Dalnoki-Veress. The glass transition in thin polymer films. *Adv. Colloid Interface Sci.* **94** 167–95, 2001.

[66] M. D. Ediger and J. A. Forrest. Dynamics near free surfaces and the glass transition in thin polymer films: a view to the future. *Macromolecules.* **47** 471–8, 2014.

[67] P. G. de Gennes. Conformations of polymers attached to an interface. *Macromolecules*. **13** 1069–75, 1980.

[68] P. K. Brazhnik, K. F. Freed and H. Tang. Polymer melt near a solid wall. *J. Chem. Phys*. **101** 9143–54, 1994.

[69] Z. Fakhraai and J. A. Forrest. Probing slow dynamics in supported thin polymer films. *Phys. Rev. Lett*. **95** 025701, 2005.

[70] S. Peter, H. Meyer, J. Baschnagel and R. Seemann. Slow dynamics and glass transition in simulated free-standing polymer films: a possible relation between global and local glass transition temperatures. *J. Phys.: Condens. Matter.* **19** 205119, 2007.

[71] J. Baschnagel and F. Varnik. Computer simulations of supercooled polymer melts in the bulk and in-confined geometry. *J. Phys.: Condens. Matter.* **17** R851–953, 2005.

[72] J-L. Barrat, J. Baschnagel and A. Lyulin. Molecular dynamics simulations of glassy polymers. *Soft Matter*. **6** 3430–17, 2010.

[73] C. Batistakis, A. V. Lyulin and M. A. J. Michels. Slowing down versus acceleration in the dynamics of confined polymer films. *Macromolecules*. **45** 7282–92, 2012.

[74] C. Batistakis, M. A. J. Michels and A. V. Lyulin. Glassy boundary layers versus enhanced mobility in capped polymer films. *J. Chem. Phys.* **139** 024906, 2013.

[75] R. P. White and J. E. G. Lipson. Polymer free volume and its connection to the glass transition. *Macromolecules*. **49** 3987–4007, 2016.

[76] T. G. Fox and P. J. Flory. 2nd-Order Transition Temperatures and Related Properties of Polystyrene 0.1. Influence of Molecular Weight. *J. Appl. Phys.* **21** 581−591, 1950.

[77] T. G. Fox and P. J. Flory Further Studies on the Melt Viscosity of Polyisobutylene. *J. Phys. Chem.* **55** 221−234, 1951.

[78] T. G. Fox and P. J. Flory. The Glass Temperature and Related Properties of Polystyrene - Influence of Molecular Weight. *J. Polym. Sci.* **14** 315−319, 1954.

[79] S. M. Aharoni. Thermal Dilatation of Polymers. *J. Macromol. Sci., Part B: Phys.* **9** 699−731, 1974.

[80] K. Dalnoki-Veress, J. A. Forrest, P. G. de Gennes and J. R. Dutcher. Glass transition reductions in thin freely-standing polymer films: a scaling analysis of chain confinement effects*. J. Phys. IV*. **10** 221–6, 2000.

[81] P. G. de Gennes. Glass transitions of freely suspended polymer films. *C. R. Acad. Sci. IV.* **1** 1179–86, 2000.

[82] S. Kim and J. M. Torkelson. Distribution of glass transition temperatures in free-standing, nanoconfined polystyrene films: a test of de gennes' sliding motion mechanism. *Macromolecules*. **44** 4546–53, 2011.

[83] S. Kawana and R. A. L. Jones. Character of the glass transition in thin supported polymer films. *Phys. Rev. E.* **63** 021501, 2001.

[84] Z. Fakhraai and J. A. Forrest. Measuring the surface dynamics of glassy polymers. Science. **319** 600–4, 2008.

[85] W. Xia, D. D. Hsu and S. Keten. Molecular Weight Effects on the Glass Transition and Confinement Behavior of Polymer Thin Films. *Macromol. Rapid. Commun*. **36**, 1422−1427, 2015.

[86] Y. Zhang and Z. Fakhraai. Decoupling of surface diffusion and relaxation dynamics of molecular glasses. *Proc. Natl. Acad. Sci USA.* **114** 4915–4919, 2017

[87] I. Langmuir. The constitution and fundamental properties of solids and liquids. Part I. Solids. *J. Am. Chem. Soc.* **38** 2221-2295, 1916.

[88] S. Brunauer, P. H. Emmett, and E. Teller. Adsorption of Gases in Multimolecular Layers. *J. Am. Chem. Soc.* **60** 309-319, 1938.

[89] E. Hecht. *Optics (4th ed.)*. Addison Wesley, 2002.

[90] D. Elson, E. Magde. Fluorescence correlation spectroscopy. I. Conceptual basis and theory. *Biopolymers*. **13** 1-27, 1974.

[91] E. Elson, D. Magde, and W. W. Webb. Fluorescence correlation spectroscopy. II. An experimental realization. *Biopolymers*. **13** 29-61, 1974.

[92] E. Elson, D. Magde, and W. W. Webb. Thermodynamic Fluctuations in a Reacting System - Measurement by Fluorescence Correlation Spectroscopy. *Phys. Rev. Lett*. **29** 705-708, 1972.

[93] R. Rigler, U. Mets, J. Widengren, and P. Kask. Fluorescence correlation spectroscopy with high count rate and low background analysis of translational diffusion. *Eur. Biophys. J.* **22** 169-175, 1993.

[94] J. Li, C. Dong and J. Ren. Strategies to reduce detection volume of fluorescence correlation spectroscopy (FCS) to realize physiological concentration measurements. *Trends Anal. Chem*. **89** 181-189, 2017.

[95] L. Sigaut, C. Villarruel, M. L. Ponce and S. P. Dawson. Fluorescence correlation spectroscopy experiments to quantify free diffusion coefficients in reaction-diffusion systems: The case of Ca2+ and its dyes. *Phys. Rev. E*. **95** 062408, 2017.

[96] B. Pelaz, P. del Pino, P. Maffre, R. Hartmann, M. Gallego, S. Rivera-Fernández, J. M. de la Fuente, G. U. Nienhaus and W. J. Parak. Surface Functionalization of Nanoparticles with Polyethylene Glycol: Effects on Protein Adsorption and Cellular Uptake. *ACS Nano*. **9** 6996-7008, 2015.

[97] I-H. Lee, S. Saha, A. Polley, H. Huang, S. Mayor, M. Rao and J. T. Groves. Live Cell Plasma Membranes Do Not Exhibit a Miscibility Phase Transition over a Wide Range of Temperatures. *J. Phys. Chem. B.* **119** 4450-4459, 2015.

[98] M. Minsky. Microscopy apparatus. Patent Number: US3013467, 1961.

[99] M. Minsky. Memoir on Inventing the Confocal Scanning Microscope. *Scanning*. **10** 128-138, 1988.

[100] O. Krichevsky, G. Bonnet. Fluorescence correlation spectroscopy: the technique and its applications. *Rep. Prog. Phys*. **65** 251-297, 2001.

[101] J. A. Roetling. Yield stress behaviour of poly(ethyl methacrylate) in the glass transition region. *Polymer*. **6** 615-169, 1965.

[102] P. J. Flory. *Principles of Polymer Chemistry*. Cornell University Press, 1953.

[103] G. D. Parfitt and C. H. Rochester. *Adsorption from Solution at the Solid/Liquid Interfaces*, chapter Adsorption of Small Molecules, pages 3-48. Academic Press, 1983.

[104] T. Sato and R. Ruch. *Stabilization of Colloidal Dispersions by Polymer Adsorption*. Marcel Dekker Ltd, 1980.

[105] P.-G. de Gennes. *Scaling Concepts in Polymer Physics*. Cornell University Press, 1979.

[106] T. Miyazaaki, R. Inoune, K. Nishida and T. Kanaya. X-ray reflectivity studies on glass transition of polystyrene thin films. *Eur. Phys. J. Special Topics*. **141** 203-206, 2007.

[107] S. Ogawa and I. Takahashi. *Biochemistry, Genetics and Molecular Biology: Carboyhydates*. Chapter 6: Glass Transition of Ultrathin Sugar Films Probed by X-Ray Reflectivity, 115-130. Intech, 2017.

[108] C.H. Park, J.H. Kim, M. Ree, B.-H. Sohn, J.C. Jung, W.-C. Zin. Thickness and composition dependence of the glass transition temperature in thin random copolymer films. *Polymer*. **45** 4507-4513, 2004.

[109] C. Yang, R. Onitsuka and I. Takahashi. Confinement effects on glass transition temperature, transition breadth, and linear expansivity: An unltraslow X-ray reflectivity study on supported ultrathin polystyrene films. *Eur. Phys. J. E.* **36** 66, 2013.

[110] F. Bloch. Nuclear Induction. *Phys. Rev*. **70** 460-474, 1946.

[111] E. M. Purcell, H. C. Torrey, R. V. Pound. Resonance Absorption by Nuclear Magnetic Moments in a Solid. *Phys. Rev.* **69** 37-38, 1946.

[112] E. L. Hahn. Spin Echoes. *Phys. Rev*. **80** 580-594, 1950.

[113] E. O. Stejskal. Use Of Spin Echoes In A Pulsed Magnetic-Field Gradient To Study Anisotropic Restricted Diffusion And Flow. *J. Chem. Phys*. **143** 3597-3599, 1965.

[114] K. F. Morris, C. S. Johnson. Diffusion-Ordered 2-Dimensional Nuclear Magnetic-Resonance Spectroscopy. *J. Am. Chem. Soc.* **114** 3139-3141, 1992.

[115] E. O. Stejskal and J. E. Tanner. Spin diffusion measurements: spin echoes in the presence of a time-dependent field gradient. *J. Chem. Phys.* **42** 288, 1965.

[116] O. Almora, C. Aranda, I. Zarazua, A. Guerrero and G. Garcia-Belmonte. Noncapacitive Hysteresis in Perovskite Solar Cells at Room Temperature. *ACS Energy Lett.* **1** 209-215, 2016.

[117] D. B. Hall, P. Underhill and J. M. Torkelson. Spin coating of thin and ultrathin polymer films. *Polym. Eng. Sci.* **38** 2039–2045, 1998.

[118] C. J. Lawrence. The mechanics of spin coating of polymer films. *Phys. Fluids.* **31** 2786, 1988.

[119] P. D. Fowler, C. Ruscher, J. D. McGraw, J. A. Forrest and K. Dalnoki-Veress. Controlling the Marangoni-induced instabilities in spin-cast polymer films: How to prepare uniform films. *Eur. Phys. J. E.* **39** 90, 2016.

[120] J. Perlich, V. Körstgens, E. Metwalli, L. Schulz, R. Georgii and P. Müller-Buschbaum. Solvent content in thin spin-coated polystyrene homopolymer films. *Macromolecules*. **42** 337-344, 2009.

[121] D. L. Gil and D. Windover. Limitations of x-ray reflectometry in the presence of surface contamination. *J. Phys. D: Appl. Phys.* **45** 235301, 2012.

[122] C. Beaucage, R. Composto and R. S. Stein. Ellipsometric study of the glass transition and thermal expansion coefficients of thin polymer films. *J. Polym. Sci. B: Polym. Phys.* **31** 319-326, 1993.

[123] J. E. Pye and C. B. Roth. Above, below and in-between the two glass transitions of ultrathin free-standing polystyrene films: thermal expansion coefficient and physical aging. *J. Polym. Sci. B: Polym. Phys.* **53** 64, 2015.

[124] E. C. Glor, G. V. Angrand and Z. Fakhraai. Exploring the broadening and the existence of two glass transitions due to competing interfacial effects in thin, supported polymer films. *J. Phys. Chem.* **146** 203330, 2017.

[125] S. Kawana and R. A. L. Jones. Effect of physical ageing in thin glassy polymer films. *Eur. Phys. J. E*. **10** 223-230, 2003.

[126] M. M. Mok, J. Kim, S. R. Marrou and J. M. Torkelson. Ellipsometry measurements of glass transition breadth in bulk films of random, block, and gradient copolymers. *Eur. Phys. J. E.* **31** 239-252, 2010.

[127] S. Kim, S. A. Hewlett, C. B. Roth and J. M. Torkelson. Confinement effects on glass transition temperature, transition breadth, and expansivity: Comparison of ellipsometry and fluorescence measurements on polystyrene films. *Eur. Phys. J. E.* **30** 83-92, 2009.

[128] P. D. Condo and K. P. Johnston. In situ measurement of the glass transition temperature of polymer with compressed fluid diluents. *J. Poly. Sci. B: Poly. Phys*. **32** 523-533, 1994.

[129] M. Mears. *Diffusion of macromolecules in confined environments*. PhD thesis. University of Sheffield, 2011.

[130] S. A. Sukhishvili, Y. Chen, J. D. Muller, E. Gratton, K. Schweizer and S. Granick. Surface diffusion of poly(ethylene glycol). *Macromolecules*. **35** 1776-1784, 2002.

[131] L. A. Utracki. *Polymer Alloys and blends: thermodynamics and rheology*. Carl Hanser Germany, 1990.

[132] J. A. Zawada, C. M. Ylitalo, G. G. Fuller, R. H. Colby, and T. E. Long. Component Relaxation Dynamics in a Miscible Polymer Blend: Poly(ethylene oxide)/Poly(methyl methacrylate). *Macromolecules*. **25** 2896-2902, 1992.

[133] M. Dionisio, A. C. Fernandes, J. F. Mano, N. T. Correia, and R. C. Sousa. Relaxation studies in PEO/PMMA Blends. *Macromolecules*. **33** 1002-1011, 2000.

[134] T. Kihara, J. Ito and J. Miyake. Measurement of Biomolecular Diffusion in Extracellular Matrix Condensed by Fibroblasts Using Fluorescence Correlation Spectroscopy. *PLoS*. **8** E82382, 2013.

[135] P. O. Gendron, F. Avaltroni and K. J. Wilkinson. Diffusion coefficients of several rhodamine derivatives as determined by pulsed field gradient-nuclear magnetic resonance and fluorescence correlation spectroscopy. *J. Fluoresc.* **18** 1093-1101, 2008.